Methods for cluster cosmology and application to the SDSS in preparation for DES Year 1 release

M. Costanzi,[1,2]* E. Rozo,[3]* M. Simet,[4] Y. Zhang [ORCID],[5] A. E. Evrard [ORCID],[6,7] A. Mantz [ORCID],[8] E. S. Rykoff,[8,9] T. Jeltema,[10] D. Gruen [ORCID],[8,9] S. Allen,[11] T. McClintock [ORCID],[3] A. K. Romer,[12] A. von der Linden,[13] A. Farahi [ORCID],[14] J. DeRose,[8,11] T. N. Varga,[15,30] J. Weller,[15,16,30] P. Giles,[12] D. L. Hollowood,[10] S. Bhargava,[12] A. Bermeo-Hernandez,[12] X. Chen,[7] T. M. C. Abbott,[17] F. B. Abdalla,[18,19] S. Avila,[20] K. Bechtol,[21] D. Brooks,[18] E. Buckley-Geer,[5] D. L. Burke,[8,9] A. Carnero Rosell,[22,23] M. Carrasco Kind,[24,25] J. Carretero,[26] M. Crocce,[27,28] C. E. Cunha,[8] L. N. da Costa,[22,23] C. Davis,[8] J. De Vicente,[29] H. T. Diehl,[5] J. P. Dietrich,[16,30] P. Doel,[18] T. F. Eifler,[31,32] J. Estrada,[5] B. Flaugher,[5] P. Fosalba,[27,28] J. Frieman,[5,33] J. García-Bellido,[34] E. Gaztanaga,[27,28] D. W. Gerdes,[6,7] T. Giannantonio,[4,30,35,36] R. A. Gruendl,[24,25] J. Gschwend,[22,23] G. Gutierrez,[5] W. G. Hartley,[18,37] K. Honscheid,[38,39] B. Hoyle,[15,30] D. J. James,[40] E. Krause,[31] K. Kuehn,[41] N. Kuropatkin,[5] M. Lima,[22,42] H. Lin,[5] M. A. G. Maia,[22,23] M. March,[43] J. L. Marshall,[44] P. Martini,[38,45] F. Menanteau,[24,25] C. J. Miller,[6,7] R. Miquel,[26,46] J. J. Mohr,[16,15,30] R. L. C. Ogando,[22,23] A. A. Plazas,[32] A. Roodman,[8,9] E. Sanchez,[29] V. Scarpine,[5] R. Schindler,[9] M. Schubnell,[7] S. Serrano,[27,28] I. Sevilla-Noarbe,[29] E. Sheldon,[47] M. Smith,[48] M. Soares-Santos,[49] F. Sobreira,[22,50] E. Suchyta,[51] M. E. C. Swanson,[25] G. Tarle,[7] D. Thomas,[20] R. H. Wechsler[8,9,11] and (DES Collaboration)

Affiliations are listed at the end of the paper

ABSTRACT

We implement the first blind analysis of cluster abundance data to derive cosmological constraints from the abundance and weak lensing signal of redMaPPer clusters in the Sloan Digital Sky Survey (SDSS). We simultaneously fit for cosmological parameters and the richness–mass relation of the clusters. For a flat Λ cold dark matter cosmological model with massive neutrinos, we find $S_8 \equiv \sigma_8 (\Omega_m/0.3)^{0.5} = 0.79^{+0.05}_{-0.04}$. This value is both consistent and competitive with that derived from cluster catalogues selected in different wavelengths. Our result is also consistent with the combined probes analyses by the Dark Energy Survey (DES), the Kilo-Degree Survey (KiDS), and with the cosmic microwave background (CMB) anisotropies as measured by *Planck*. We demonstrate that the cosmological posteriors are robust against variation of the richness–mass relation model and to systematics associated with the calibration of the selection function. In combination with baryon acoustic oscillation data and big bang nucleosynthesis data (Cooke et al.), we constrain the Hubble rate to be $h = 0.66 \pm 0.02$, independent of the CMB. Future work aimed at improving our understanding of the scatter of the richness–mass relation has the potential to significantly improve the precision of our cosmological posteriors. The methods described in this work were developed for use

---

* E-mail: matteo.costanzi@inaf.it (MC); erozo@email.arizona.edu (ER)

in the forthcoming analysis of cluster abundances in the DES. Our SDSS analysis constitutes the first part of a staged-unblinding analysis of the full DES data set.

Key words: galaxies: clusters: general – cosmological parameters – large-scale structure of Universe.

1 INTRODUCTION

Galaxy clusters form from the high-density peaks of the initial matter distribution. As such, they bear the imprints of the statistical properties of the matter density field and its growth (for reviews, see e.g. Allen, Evrard & Mantz 2011; Kravtsov & Borgani 2012). The abundance of galaxy clusters has been used since the late 1990s to constrain the mean matter density of the Universe, Ω_m, and the amplitude of the density fluctuations in terms of σ_8, the present-day rms of the linear density field in spheres of $8\,h^{-1}$ Mpc radii (e.g. Eke et al. 1998; Henry 2000; Borgani et al. 2001; Pierpaoli, Scott & White 2001; Reiprich & Böhringer 2002; Henry 2004, for early works). Constraints on σ_8 are especially powerful in combination with measurements of the amplitude of the matter power spectrum at high redshift – e.g. from cosmic microwave background (CMB) data – enabling us to study the growth of density perturbations over cosmic time. These studies allow us to place constraints on parameters such as the total neutrino mass, the dark energy equation of state, and parameters governing modified gravity models.

Current studies using cluster catalogues selected in the X-ray, optical, and millimetre wavelengths, provide consistent constraints on σ_8 and Ω_m (e.g. (e.g. Planck Collaboration XXIV 2016b; Vikhlinin et al. 2009; Mantz et al. 2010, 2015; Rozo et al. 2010; de Haan et al. 2016). These data have been also used in combination with H_0 and baryon acoustic oscillation (BAO) priors to place competitive constraints on the dark energy equation-of-state parameter, modification of gravity and neutrino masses (e.g. Planck Collaboration XXIV 2016b; Mantz et al. 2010, 2015; Burenin & Vikhlinin 2012; Cataneo et al. 2015; de Haan et al. 2016). Ongoing – e.g. the Dark Energy Survey (DES),[1] the Hyper Suprime-Cam[2] – and forthcoming – the Large Synoptic Survey Telescope,[3] *Euclid*,[4] eRosita[5] – wide-area surveys aim to use clusters samples with an order of magnitude more systems than previous analyses in order to improve upon current constraints.

The most critical difficulty that cluster abundance studies must confront is the fact that cluster masses are not easily measured, forcing us to rely on observational proxies that correlate with mass. Specifically, while it is possible to predict the abundance of dark matter haloes as a function of mass in an arbitrary cosmology with per cent level accuracy (e.g. Sheth & Tormen 1999; Tinker et al. 2008; Crocce et al. 2010; Bocquet et al. 2016; McClintock et al. 2019b), halo masses themselves are not directly observable. At present, cosmological constraints from cluster abundance analyses at all wavelengths are limited by the uncertainty in the calibration of the relation between the cluster mass and the observable property used as a mass proxy, be it richness (i.e. count of member galaxies), X-ray luminosity or the thermal Sunyaev–Zeldovich signal.

Currently, weak gravitational lensing measurements provide the gold-standard technique for estimating cluster masses (see e.g. von der Linden et al. 2014b, for a discussion). The weak lensing signal, i.e. the tangential alignment of background galaxies around the foreground cluster due to gravitational lensing, is a well-understood effect, sensitive to both dark and baryonic matter. Moreover, in contrast to other techniques (e.g. velocity dispersion and hydrostatic mass measurements), weak lensing mass measurements do not rely on assumptions about the dynamical state of the cluster. Despite these advantages, many sources of systematic error do affect this type of measurement, e.g. shear and photometric redshift biases, halo triaxiality, and projection effects. These systematics represent a significant amount of the total error budget of many recent studies (e.g. von der Linden et al. 2014a; Hoekstra et al. 2015; Melchior et al. 2017; Simet et al. 2017; Medezinski et al. 2018; Miyatake et al. 2019). Not surprisingly, as the statistical uncertainty continues to decrease, these systematics have come to dominate the total error budget (e.g. McClintock et al. 2019a).

In this work, we combine cluster abundances and stacked weak lensing mass measurements from the Sloan Digital Sky Survey data release 8 (SDSS DR8; Aihara et al. 2011) to simultaneously constrain cosmology and the richness–mass relation of galaxy clusters. Our cluster sample is selected using the red-sequence Matched-filter Probabilistic Percolation algorithm (redMaPPer; Rykoff et al. 2014), and the stacked weak lensing mass estimates are presented in Simet et al. (2017). The analysis is similar in spirit to that of Rozo et al. (2010) but with significant updates, particularly with regards to the modelling of the cluster selection function. Our observables are the number of clusters and the mean cluster mass in bins of richness – our mass proxy – and redshift. We explicitly account for the small cosmological dependence of the recovered weak lensing masses in our analysis. To avoid confirmation bias, the bulk of the analysis has been performed blind: the values of the cosmological parameters sampled by the Monte Carlo Markov Chains (MCMC) were randomly displaced by an amount that was unknown to us, and were shifted back only after a broad set of validation tests were passed. No changes were done to the analysis pipeline post-unblinding.[6] This is the first cluster abundance analysis to be performed blind in the cosmological parameters. The methods presented in this paper were developed for the forthcoming cosmological analysis of the DES Y1 redMaPPer cluster catalogue (DES Collaboration, in preparation).

This paper is organized as follows. In Section 2, we introduce the data used for this study. In Section 3, we present the model used to perform the cosmological analysis, including expectation values for the two observables, modelling of the systematics and likelihood model. We validate our model by means of synthetic data in Section 4. We detail our blinding procedure in Section 5.

---

[1]https://www.darkenergysurvey.org
[2]http://hsc.mtk.nao.ac.jp/ssp/
[3]https://www.lsst.org/
[4]http://sci.esa.int/euclid/
[5]http://www.mpe.mpg.de/eROSITA

[6]Ongoing work for DES has demonstrated that the adopted systematic error budget was too optimistic. Details will be presented in forthcoming work. We expect these changes will have only a minor (less than 1σ) impact on the current cosmological posteriors.

Table 1. Summary of the data and systematic corrections adopted in the analysis. We use the same redshift range, $0.1 \leq z \leq 0.3$, for all the richness bins. The second column lists the observed number counts and their uncertainties, the latter estimated as the square root of the diagonal terms of the best-fitting model covariance matrix (see Section 3.3). The numbers between parenthesis correspond to the number counts corrected for the miscentring bias factors listed in the third column (see Section 2.2). The values of the mean cluster mass reported here, $\log(\bar{M}_{200,m}^{\mathrm{WL}})$, assume $\Omega_{\mathrm{m}} = 0.30$. The two uncertainties shown correspond to the statistical and systematic error, respectively. We assume systematic errors to be fully correlated between the cluster bins. The fifth column lists the slopes that define the cosmological dependence of the weak lensing mass estimates (equation 1).

$\Delta\lambda^{\mathrm{ob}}; z \in [0.1, 0.3]$	Number counts	γ^{Misc}	$\log(\bar{M}_{200,m}^{\mathrm{WL}})$ [M$_\odot$ h^{-1}]	d$\log M^{\mathrm{WL}}$/dΩ_{m}
$[20, 27.9)$	$3604\,(3711) \pm 100$	1.030 ± 0.011	$14.111 \pm 0.024 \pm 0.026$	-0.65
$[27.9, 37.6)$	$1740\,(1788) \pm 61$	1.028 ± 0.011	$14.263 \pm 0.030 \pm 0.024$	-0.66
$[37.6, 50.3)$	$942\,(978) \pm 41$	1.039 ± 0.014	$14.380 \pm 0.033 \pm 0.026$	-0.68
$[50.3, 69.3)$	$461\,(476) \pm 27$	1.034 ± 0.015	$14.609 \pm 0.036 \pm 0.028$	-0.77
$[69.3, 140)$	$217\,(223) \pm 18$	1.028 ± 0.016	$14.928 \pm 0.029 \pm 0.036$	-0.65

The results of our analysis are presented in Sections 6 and 7. Finally, we conclude in Section 8.

2 DATA

2.1 Cluster and weak lensing catalogues

Both the cluster and weak lensing shear catalogues used in this analysis are based on the SDSS DR8 (Aihara et al. 2011). A summary of the data employed in this analysis is presented in Table 1. Throughout the paper, all masses are given in units of M$_\odot$ h^{-1}, where $h = H_0/100\,\mathrm{km\,s^{-1}Mpc^{-1}}$, and refer to an overdensity of 200 with respect to the mean. We use 'log' and 'ln' to refer to the logarithm with base 10 and e, respectively.

We use photometrically selected galaxy clusters identified in $\sim 10\,000\,\mathrm{deg^2}$ SDSS DR8 with the redMaPPer cluster finding algorithm (Rykoff et al. 2014). In brief, redMaPPer is a red-sequence cluster that iteratively self-calibrates a model for red-sequence galaxies. The observable mass proxy is the cluster richness, a probabilistic estimate of the total number of galaxies in the cluster. Typical cluster photometric redshift uncertainties are $\sigma_z/(1+z) \lesssim 0.01$ with negligible bias. Our analysis is restricted to the redshift range $z \in [0.1, 0.3]$ to ensure accurate photometry and a volume-limited catalogue. Only clusters of richness $\lambda \geq 20$ are used in our analysis, which ensures that 99 per cent of the redMaPPer galaxy clusters can be unambiguously mapped to individual dark matter haloes (Farahi et al. 2016). In this work, we use v5.10 of the SDSS redMaPPer cluster catalogue (Rozo et al. 2015).

The weak lensing mass estimates employed in this analysis are a slight update from those presented in Simet et al. (2017). They rely on the shear catalogue presented in Reyes et al. (2012), comprising ~39 million galaxies over $\sim 9000\,\mathrm{deg^2}$ of the SDSS footprint. The effective source density is $1.2\,\mathrm{gal\,arcmin^{-2}}$. Shear estimates were derived from the SDSS imaging using the re-Gaussianization algorithm of Hirata & Seljak (2003) and the appropriately calibrated responsivity to convert the measured shape distortions into shear estimates. The multiplicative shear bias appropriate for this catalogue was characterized in Mandelbaum et al. (2012, 2013, 2018). The photometric redshifts for the sources in the shear catalogue were obtained using the Zurich Extragalactic Bayesian Redshift Analyzer (Feldmann et al. 2006), and the associated systematic uncertainties were calibrated in Nakajima et al. (2012).

2.2 Cluster number counts data

Following Simet et al. (2017), we collect our galaxy clusters in five richness bins and a single redshift bin (see Table 1). The richness limits of our bins are $\lambda^{\mathrm{ob}} = [20, 27.9, 37.6, 50.3, 69.3, 140]$. The two key observational systematics in our analysis are photometric redshift errors and cluster miscentring. Photometric redshift uncertainties are forward-modelled as described in Section 3.1.

We assume that the correct centre of a galaxy cluster is always coincident with a bright cluster galaxy (though not necessarily the brightest). This assumption is motivated by the fact that modern halo finders (e.g. Behroozi, Wechsler & Wu 2013) define the centre of dark matter haloes as the position of the dominant dark matter substructure within the halo. This dominant substructure is expected to host a bright galaxy. redMaPPer identifies the central galaxy of a cluster via an iteratively self-trained matched-filter algorithm that combines luminosity and local galaxy density information. This algorithm is demonstrably superior to centring clusters on the brightest cluster-member galaxy (Hikage et al. 2018). Nevertheless, the mis-identification of the cluster centre can still occur. The uncertainty in the systematic corrections due to cluster miscentring are very nearly negligible, so rather than forward modelling them, we have opted for the simpler route of applying a correction to the observed data vector, and adding the corresponding systematic uncertainty in the abundances to the covariance matrix of the data vector.

Our miscentring correction is based on the analyses in Zhang et al. (2019) and von der Linden et al. (in preparation). To characterize the probability of a redMaPPer cluster being miscentred, we use subsamples of redMaPPer clusters with either *Chandra* or *Swift* X-ray imaging. Specifically, we compared the redMaPPer central galaxies to the X-ray derived cluster centres. Roughly speaking, in that analysis small $\lesssim100\,\mathrm{kpc}$ offsets are attributed to miscentring in the X-ray data, while large offsets are attributed to catastrophic miscentring of redMaPPer clusters. In practice, the analysis forward-models the observed miscentring distribution. We found that 71.5 ± 6 per cent of redMaPPer galaxy clusters are correctly centred. This value does not appear to exhibit a trend with richness. The result is somewhat lower than but consistent with the estimate of Hikage et al. (2018) on the basis of the weak lensing profile of redMaPPer clusters.

The radial offset distribution of the miscentred clusters is characterized using a two-dimensional Gaussian.

We characterize the impact of cluster miscentring on the cluster richness by measuring the richness of the clusters at the second most likely central galaxy. As expected, miscentring systematically underestimates cluster richnesses, albeit with some scatter. Both the bias and scatter increasing as the radial offset increases (Zhang et al. 2019).

Having characterized (i) the fraction of miscentred clusters; (ii) the distribution of radial offsets of miscentred clusters; and (iii) how the richness of a cluster changes when it is miscentred by a given radial offset, we can readily estimate the impact of miscentring on the cluster abundance function. Specifically, we assigned richness values to haloes in a numerical simulation using the model of Costanzi et al. (2018). The assigned halo richnesses are then scattered using our centring model. We compute the ratio $\gamma^{\mathrm{Misc}} = N^{\mathrm{cent}}/N^{\mathrm{miscent}}$ between N^{cent}, the number of clusters in a bin in the absence of miscentring, and N^{miscent}, the number of clusters in a bin including the impact of miscentring. We apply the $\gamma^{\mathrm{Misc}} \sim 1.030$ (see Table 1) systematic correction to the number of galaxy clusters we observe in our Monte Carlo experiment, and add the corresponding covariance matrix to the covariance matrix of the cluster counts. The uncertainty associated with cluster miscentring in the abundance function is ≈ 1.3 per cent. That is, cluster miscentring is subdominant to Poisson noise in all richness bins, and easily subdominant to the uncertainty in our calibration of the richness–mass relation.

The shaded regions in the top-left panel of Fig. 1 shows the miscentring-corrected cluster abundances. The width of the regions along the y-axis is set by the diagonal entries of the corresponding covariance matrix, whereas their width along the x-axis reflects the width of the richness bin. Our best-fitting model is shown as the blue points. The bottom-left panel shows the corresponding per cent residuals.

2.3 Weak lensing cluster masses

We calculate the mean mass of clusters in a richness bin using the stacked weak lensing mass profiles of the clusters as described in Simet et al. (2017). These profiles are modelled using a Navarro, Frenk, and White profile (NFW; Navarro, Frenk & White 1997), accounting for the effects of cluster miscentring, halo triaxiality, and projection effects. The concentration of the best-fitting NFW profiles is modelled using the mass–concentration relation presented in Diemer & Kravtsov (2015) with a free parameter for the amplitude.

In this work, we follow the methodology of Simet et al. (2017) to estimate the mean cluster mass in each bin with three critical exceptions:

(i) We correct for the 3 ± 3 per cent multiplicative shear bias due to undetected blends that was first identified in Mandelbaum et al. (2018).

(ii) We update the centring priors employed in the weak lensing analysis based on the work of Zhang et al. (2019) and von der Linden et al. (in preparation) described above. The radial offset of miscentred clusters is described by a two-dimensional Gaussian of width $\tau = (0.29 \pm 0.04)R_\lambda$, where R_λ is the cluster radius assigned by redMaPPer.

(iii) Rather than simultaneously modelling all galaxy clusters to derive a scaling relation that describes all richness bins, we estimate the mean mass of each individual richness bin.

The mean cluster mass in a bin is estimated by fitting a scaling relation with scatter to each bin independently, and using the poste-

riors to calculate the mean mass. The result is weakly dependent on the assumed scatter in the mass–richness relation, with a degeneracy of the form $\log\langle M|\lambda, \sigma\rangle = \log M + 0.06\sigma_{\ln M|\lambda}^2$. That is, varying $\sigma_{\ln M|\lambda}$ over the range [0.0, 0.5] modifies the recovered log-masses by an amount ranging from 0 to 0.015. We adopt a fiducial correction of 0.007 ± 0.007.

Following the analysis described in Simet et al. (2017, see section 5.5), we further estimate the systematic uncertainty in our weak lensing masses due to modelling the lensing profile with a pure NFW halo, without accounting for a two-halo term, or due to deviations from the NFW profile (e.g. Diemer & Kravtsov 2014). The recovered biases for each of our richness bins varies from 2 per cent on the low-mass end to 3 per cent on the high-mass end. We apply these corrections to our data, and assign a systematic uncertainty on this correction equal to half the magnitude of the correction.

Since our final cosmological constraints are limited by systematic uncertainties in mass calibration, we summarize our observational error budget in Table 2. For details of how these are determined, we refer the reader to Simet et al. (2017). Our results are summarized in Table 1, where we collect the best weak lensing estimates for the mean mass of the galaxy clusters in each richness bin. The logarithm of the mean mass, $\log \bar{M}$, for each of our five richness bins is shown in the top-right panel of Fig. 1, along with the best-fitting model from our cosmological analysis. The bottom-right panel shows the corresponding residuals.

As in Simet et al. (2017), we characterize the dependence of the recovered weak lensing masses on Ω_{m} via a simple power law,

$$\log \bar{M}^{\mathrm{WL}}(\Omega_{\mathrm{m}}) = \left. \log \bar{M}^{\mathrm{WL}}\right|_{\Omega_{\mathrm{m}}=0.3} + \left(\frac{\mathrm{d}\log M^{\mathrm{WL}}}{\mathrm{d}\Omega_{\mathrm{m}}}\right)(\Omega_{\mathrm{m}} - 0.3).$$

(1)

The slopes have been obtained by fitting equation (1) to the weak lensing masses estimated assuming a grid of fiducial Ω_{m} values ranging from $\Omega_{\mathrm{m}} = 0.24$ to $\Omega_{\mathrm{m}} = 0.36$ while setting $\Omega_\Lambda = 1 - \Omega_{\mathrm{m}}$. The resulting slopes are listed in Table 1, and are used in our cosmological analysis to rescale $\log \bar{M}^{\mathrm{WL}}$ at each step of the MCMC by the appropriate Ω_{m} value.[7]

3 THEORY AND METHODS

In what follows, all quantities labelled with 'ob' denote quantities inferred from observation, while quantities labelled with 'true' indicate intrinsic halo properties. $P(Y|X)$ denotes the conditional probability of Y given X.

3.1 Expectation values

3.1.1 Base model

Let $\Delta\lambda_i^{\mathrm{ob}}$ denote richness bin i, and Δz_j^{ob} denote the redshift bin j. The expectation value of the number of galaxy clusters $N(\Delta\lambda_i^{\mathrm{ob}}, \Delta z_j^{\mathrm{ob}})$ is given by

$$\langle N(\Delta\lambda_i^{\mathrm{ob}}, \Delta z_j^{\mathrm{ob}})\rangle = \int_0^\infty \mathrm{d}z^{\mathrm{true}} \, \Omega_{\mathrm{mask}}(z^{\mathrm{true}}) \frac{\mathrm{d}V}{\mathrm{d}z^{\mathrm{true}}\mathrm{d}\Omega}(z^{\mathrm{true}})$$
$$\times \langle n(\Delta\lambda_i^{\mathrm{ob}}, z^{\mathrm{true}})\rangle \int_{\Delta z_j^{\mathrm{ob}}} \mathrm{d}z^{\mathrm{ob}} \, P(z^{\mathrm{ob}}|z^{\mathrm{true}}, \Delta\lambda_i^{\mathrm{ob}}),$$

(2)

---

[7]Our posterior extends to matter densities below $\Omega_{\mathrm{m}} = 0.24$. We verified a posteriori that the linear matter density scaling extends to $\Omega_{\mathrm{m}} = 0.15$.
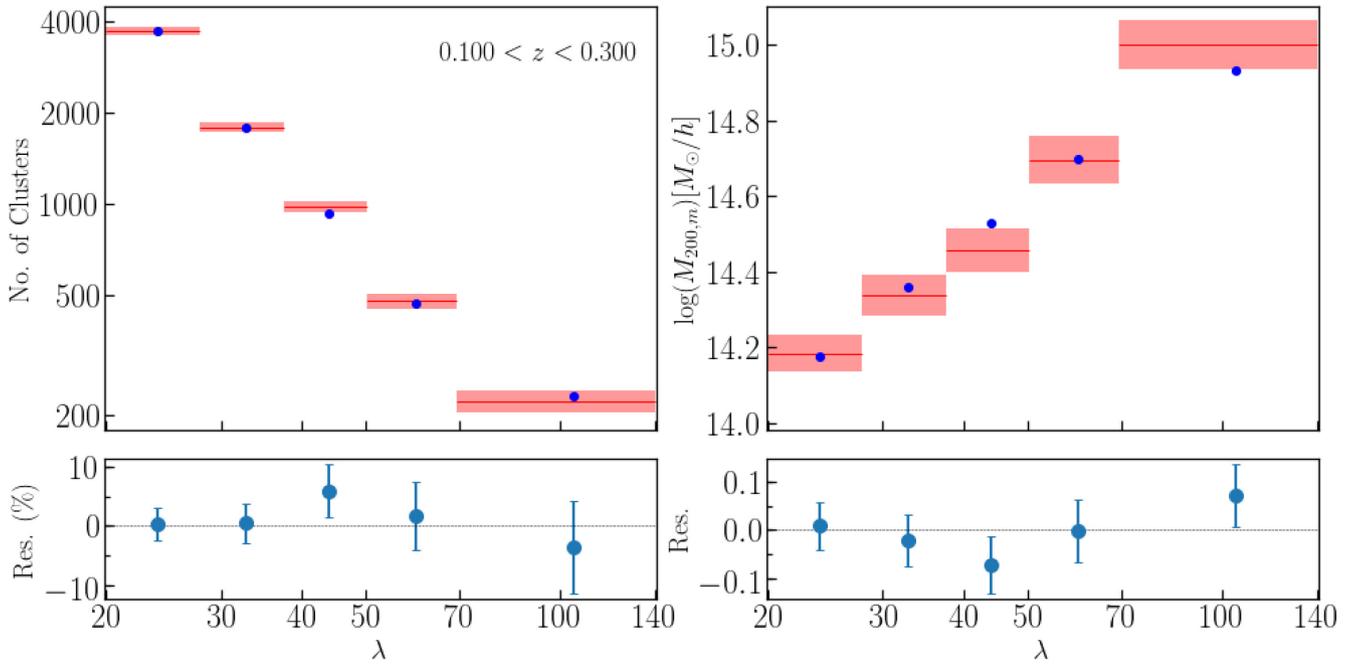
Figure 1. Observed (*shaded area*) and best-fitting model (*dots*) of cluster number counts (*left-hand* panel) and mean cluster masses (*right-hand* panel) in the five richness bins considered. The model predictions have been computed as described in Section 3 using the best-fitting values derived from our analysis. The *y* extent of the *shaded* areas is given by the square root of the diagonal terms of the corresponding covariance matrix. The lower panels show the per cent residual (*left*) and the residual (*right*) of our best-fitting model to the data.

Table 2. Error budget for the weak lensing mass calibration data used in our cosmological analysis. The 'Gaussian equivalent' error for top-hat systematics refers to the square root of the variance of the top-hat prior of the appropriate effect. For instance, a Gaussian prior for shear and photo-*z* biases of ± 2.8 per cent has the same variance as a top-hat prior of ± 5 per cent. The statistical error quoted in the table refers to the uncertainty in the amplitude of the mass–richness relation. The statistical uncertainty on any individual mass estimate is larger.

Source	Associated error
Shear and photo-*z* bias	6.5 per cent top-hat (3.8 per cent Gaussian equivalent)
Source blending	3.9 per cent top-hat (2.3 per cent Gaussian equivalent)
Cluster triaxiality and projections	3 per cent Gaussian
Cluster centring	≤ 1 per cent
Modelling systematics	2.0 per cent Gaussian (richness dependent)
Scatter corrections	1.6 per cent Gaussian
Total systematic error	6.0 per cent Gaussian
Statistical error	4.8 per cent Gaussian
Total	7.7 per cent

where $dV/(dz^{\text{true}} d\Omega)$ is the comoving volume element per unit redshift and solid angle, and $\Omega_{\text{mask}}(z^{\text{true}})$ is the effective survey area at redshift z. The survey area depends on redshift because galaxy clusters are not point-like: whether a cluster is formally within the survey area or not depends not just on the location of the galaxy cluster in the sky, but also on how the survey boundaries (including star holes and any other masked regions) intersect the projected area of the cluster in the sky. To estimate the survey area, we randomly place clusters in the sky, and compute the fraction of the galaxy cluster that does not fall within the survey footprint. The footprint of the cluster survey is defined by the collection of all points for which at least 80 per cent of the cluster falls within the photometric survey boundaries. This 80 per cent criterion is the fiducial choice for all redMaPPer runs, and is chosen as a compromise between requiring clusters not be heavily masked, and losing a minimal amount of

area due to masking. In principle, this masking criteria implies that the survey area depends on cluster richness (via the scale radius R_λ), but we find this dependence to be negligible (≤ 1 per cent over the redshift range $z \in [0.1, 0.3]$ employed in this study).

The second integral of equation (2) accounts for the uncertainty in the photometric redshift estimate. We model $P(z^{\text{ob}}|z^{\text{true}}, \Delta\lambda_i^{\text{ob}})$ – the probability of assigning to a cluster at redshift z^{true} a photometric redshift z^{ob} – with a Gaussian distribution having mean z^{true} and a redshift and richness-dependent variance. The variance is set by the reported photometric redshift uncertainty in the redMaPPer cluster catalogue. Specifically, we fit a third-order polynomial to the redMaPPer photometric redshift errors as a function of redshift for galaxy clusters in each of our five richness bins (we find this is sufficient to fully describe our data). Photometric redshift uncertainties range from ≈ 0.005 at $z \approx 0.15$ to ≈ 0.014 at $z \approx 0.3$,

with richer clusters having somewhat smaller photometric redshift uncertainties than low-richness clusters.

As shown in fig. 9 of Rykoff et al. (2014), the redMaPPer photometric redshifts are excellent: they are nearly unbiased, and the reported photometric redshift uncertainties are both small and accurately describe the width of the photometric redshift offsets relative to the spectroscopic cluster redshifts (where available). Using the specific cluster sample employed in this work ($\lambda \geq 20$, $z \in [0.1, 0.3]$), we evaluate the systematic bias of the redMaPPer photometric redshift by fitting a Gaussian distribution to the redshift offset $z_\lambda - z_{\rm spec}$, where z_λ is our photometric cluster redshift estimate, and $z_{\rm spec}$ is the spectroscopic redshift of the central galaxy assigned to the cluster (when available). We find a mean bias of 0.002, i.e. $z_\lambda = z_{\rm spec} + 0.002$. Likewise, from a Gaussian fit to the distribution of scaled errors $(z_\lambda - z_{\rm spec})/\sigma_z$ we find that the reported photometric redshift uncertainties in redMaPPer should be boosted by a factor of 1.014. In both cases, the statistical uncertainties in the estimates are negligible. We have verified that the above systematic are unimportant by running two versions of our analysis, one without applying these corrections, and one after applying these corrections. The resulting posteriors are nearly identical. For specificity, from here on out we apply the above corrections, that is, we set $\langle z^{\rm ob}|z^{\rm true}\rangle = z^{\rm true} + 0.002$ and increase the photometric redshift errors by a factor of 1.014.

Finally, $\langle n(\Delta\lambda_i^{\rm ob}, z^{\rm true})\rangle$ in equation (2) is the expected number density of haloes in the richness bin $\Delta\lambda_i^{\rm ob}$. This quantity is given by

$$\langle n(\Delta\lambda_i^{\rm ob}, z^{\rm true})\rangle = \int_0^\infty {\rm d}M\, n(M, z^{\rm true}) \int_{\Delta\lambda_i^{\rm ob}} {\rm d}\lambda^{\rm ob}\, P(\lambda^{\rm ob}|M, z^{\rm true}),$$
(3)

where $P(\lambda^{\rm ob}|M, z^{\rm true})$ denotes the probability that a halo of mass M at redshift $z^{\rm true}$ is observed with a richness $\lambda^{\rm ob}$ (see Section 3.1.2) and $n(M, z^{\rm true})$ is the halo mass function that is assumed to follow the form of Tinker et al. (2008):

$$n(M, z) = \frac{3}{4\pi R^3(M)} \frac{{\rm d}\ln\sigma(M)^{-1}}{{\rm d}M} f^{\rm Tinker}(\sigma(M), z).$$
(4)

Several studies have explored how the mass function from *N*-body simulations should be extended in order to incorporate the effects of massive neutrinos (e.g. Brandbyge et al. 2010; Castorina et al. 2014; Villaescusa-Navarro et al. 2014; Liu et al. 2018). A common finding of these studies is that massive neutrinos play a negligible role in the collapse of dark matter haloes, while they suppress the growth of matter density fluctuations on scales smaller than the neutrino free-streaming length. Here, we account for these effects following the prescription of Costanzi et al. (2013): (i) we neglect the density neutrino component in the relation between mass and scale – i.e. $M \propto (\rho_{\rm cdm} + \rho_{\rm b})R^3$ – and (ii) use only the cold dark matter and baryon power spectrum components to compute the variance of the density field, $\sigma^2(M)$.

We can use similar arguments to the ones used to derive equation (2) to compute the expectation value for the mean mass of galaxy clusters within a specific richness and redshift bin. This is given by

$$\langle \bar{M}(\Delta\lambda_i^{\rm ob}, \Delta z_j^{\rm ob})\rangle = \left[\frac{\langle M^{\rm tot}(\Delta\lambda_i^{\rm ob}, \Delta z_j^{\rm ob})\rangle}{\langle N(\Delta\lambda_i^{\rm ob}, \Delta z_j^{\rm ob})\rangle} \right],$$
(5)

i.e. the ratio of the expected total mass inside the bin over the total number of clusters inside said bin (equation 2). Note that observationally, we stack $\Delta\Sigma$, not M, and since the two are not

linearly related to each other – $\Delta\Sigma$ is proportional to the integrated mass density profile – it is not necessarily the case that the recovered weak lensing mass is identical to the mean mass of the clusters. However, we use simulations to calibrate the relation between the recovered weak lensing mass and the mean mass in a bin to properly account for this effect.

The total mass of all clusters in a bin is calculated via

$$\langle M^{\rm tot}(\Delta\lambda_i^{\rm ob}, \Delta z_j^{\rm ob})\rangle = \int_0^\infty {\rm d}z^{\rm true}\, \Omega_{\rm mask} \frac{{\rm d}V}{{\rm d}z^{\rm true}{\rm d}\Omega}(z^{\rm true})$$
$$\times \langle Mn(\Delta\lambda_i^{\rm ob}, z^{\rm true})\rangle \int_{\Delta z_j^{\rm ob}} {\rm d}z^{\rm ob}\, P(z^{\rm ob}|z^{\rm true}),$$
(6)

where the total mean mass per unit volume in the *i*th richness bin is given by

$$\langle Mn(\Delta\lambda_i^{\rm ob}, z^{\rm true})\rangle = \int_0^\infty {\rm d}M\, Mn(M, z^{\rm true})$$
$$\times \int_{\Delta\lambda_i^{\rm ob}} {\rm d}\lambda^{\rm ob}\, P(\lambda^{\rm ob}|M, z^{\rm true}).$$
(7)

In practice, the integrals over the observed redshift in the numerator and denominator of equation (5) are each weighted by the appropriate weak lensing weight per clusters $w_{\rm WL}(z)$, where w is the mean weight applied to sources as a function of redshift – $w \propto \langle\Sigma_{\rm crit}^{-1}\rangle^2/(1 + z)^2$ – times the number of sources per cluster. We have found including this weight changes the predicted masses by less than 1 per cent. Nevertheless, our fiducial result includes this additional redshift weighting.

3.1.2 The observed richness–mass relation

Turning to the probability distribution $P(\lambda^{\rm ob}|M, z^{\rm true})$, in addition to the stochastic nature of the relation between cluster richness and halo mass, the observed richness of a galaxy cluster is subject to projection effects. Indeed, there are now multiple lines in support of the existence of projection effects in the SDSS redMaPPer cluster catalogue (Farahi et al. 2016; Busch & White 2017; Zu et al. 2017; Sohn et al. 2018). Following Costanzi et al. (2018), we model $P(\lambda^{\rm ob}|M, z^{\rm true})$ as the convolution of two probability distributions:

$$P(\lambda^{\rm ob}|M, z^{\rm true}) = \int_0^\infty {\rm d}\lambda^{\rm true}\, P(\lambda^{\rm ob}|\lambda^{\rm true}, z^{\rm true})P(\lambda^{\rm true}|M, z). \quad (8)$$

The first term inside the integral accounts for projection effects and observational noise in the richness estimates. The second term inside the integral accounts for the stochastic relation between halo mass and the intrinsic halo richness $\lambda^{\rm true}$.

Below, we start describing the model adopted for the intrinsic richness–mass relation $P(\lambda^{\rm true}|M, z)$. The probability distribution $P(\lambda^{\rm ob}|\lambda^{\rm true}, z^{\rm true})$ was the focus of a detailed numerical study in a companion paper (Costanzi et al. 2018). A brief overview of that work is presented in the subsequent subsection.

The intrinsic richness–mass relation: Different parametrizations for $P(\lambda^{\rm true}|M, z)$ have been proposed in the literature, typically assuming a lognormal distribution with the expectation value for the richness modelled as a power law (see e.g. Rozo et al. 2010; Mana et al. 2013; Murata et al. 2018). In this analysis, we opt for a model that more closely resembles halo occupation distribution functions typically used to study galaxy clustering (Berlind & Weinberg 2002; Bullock, Wechsler & Somerville 2002). A recent review of halo occupation modelling and other approaches to modelling the

galaxy–halo connection can be found in Wechsler & Tinker (2018) (see also e.g. the discussion in section 4 of Jiang & van den Bosch 2016 and appendix D of Reddick et al. 2013). The total richness of a halo of mass M is given by $\lambda^{\mathrm{true}} = \lambda^{\mathrm{cent}} + \lambda^{\mathrm{sat}}(M)$, where λ^{cent} is the number of central galaxies (either zero or unity), and λ^{sat} is the number of satellite galaxies in the cluster (Kravtsov et al. 2004; Zheng et al. 2005). We model the expectation value of λ^{cent} as a step function, $\langle\lambda^{\mathrm{cent}}|M\rangle = 1$ for $M \geq M_{\mathrm{min}}$, and $\langle\lambda^{\mathrm{cent}}|M\rangle = 0$ otherwise. While in practice these step functions have a finite width, we expect all clusters in our sample to have masses $M \gg M_{\mathrm{min}}$, so that the step-function approximation should be easily sufficient.

Turning to the satellite galaxy population, it has long been known that the scatter in the number of satellites is super-Poissonian at large occupations numbers (Boylan-Kolchin et al. 2010), but is close to Poissonian otherwise. More recently, the number of satellites has been shown to be sub-Poissonian at very low occupancy (Mao, Williamson & Wechsler 2015; Jiang & van den Bosch 2016). Since we are interested in galaxy clusters, we ignore this small deviation from Poisson statistics at low N in our analysis. We add variance to a Poisson distribution by modelling $P(\lambda^{\mathrm{sat}}|M)$ as the convolution of a Poisson distribution with a Gaussian distribution. Operationally, this is equivalent to assuming the number of satellite galaxies in a halo of mass M is a Poisson realization of some expectation value μ, where μ exhibits halo-to-halo scatter, e.g. due to formation history (Mao et al. 2015). We model the halo-to-halo scatter as a Gaussian with variance $\sqrt{\mathrm{Var}(\mu)} = \sigma_{\mathrm{intr}}\langle\lambda^{\mathrm{sat}}|M\rangle$. This additional halo-to-halo scatter enables us to recover the super-Poisson scatter in the halo occupation at large occupancy numbers.

In detail, the expectation value of the satellite contribution to λ^{true} is given by (Kravtsov et al. 2004; Zehavi et al. 2011)

$$\langle\lambda^{\mathrm{sat}}|M\rangle = \left(\frac{M - M_{\mathrm{min}}}{M_1 - M_{\mathrm{min}}}\right)^{\alpha},\tag{9}$$

Here, M_{min} is the minimum mass for a halo to form a central galaxy, while M_1 is the characteristic mass at which haloes acquire one satellite galaxy. Our parametrization enforces $\langle\lambda^{\mathrm{sat}}|M\rangle = 0$ when $M \leq M_{\mathrm{min}}$. Finally, the expectation value of the Gaussian component is set to zero, while the variance of the Gaussian term is set to $\sigma_{\mathrm{intr}}\langle\lambda^{\mathrm{sat}}|M\rangle$.

The convolution of a Poisson distribution with a Gaussian distribution does not have an analytic closed form. However, we have found that a skew-normal distribution is an excellent approximation to the resulting distribution. Its model parameters – skewness and variance – depend on $\langle\lambda^{\mathrm{sat}}|M\rangle$ and σ_{intr}, and are obtained by fitting the skew-normal model to the appropriate Gaussian–Poisson convolution (see Appendix B). By creating a lookup table for these parameters, we can avoid having to numerically compute the convolution of the Poisson and Gaussian distributions, significantly increasing the computational efficiency of our model. In Section 6.2, we discuss how our choice of parametrization impacts the cosmological constraints derived from the SDSS redMaPPer sample.

Modelling observational scatter in richness estimates: The scatter in the distribution $P(\lambda^{\mathrm{ob}}|\lambda^{\mathrm{true}})$ is due to observational scatter, i.e. noise on the estimated richness values due to photometric noise, uncertainties in background subtraction, and projection/percolation effects. The latter refers to the boosting of the richness of a cluster due to member galaxies of other structures along the line of sight that are mistakenly associated with it (projections), and the resulting loss of associated member galaxies for the masked clusters (percolation). In Costanzi et al. (2018), we developed a formalism that quantitatively characterizes these effects, demonstrated the
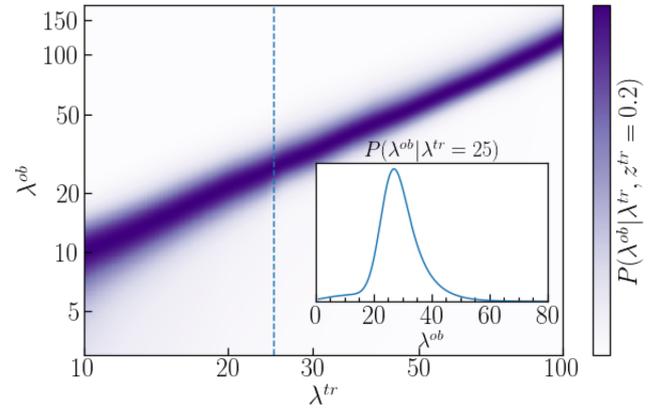

Figure 2. $P(\lambda^{\mathrm{ob}}|\lambda^{\mathrm{true}})$ as a function of the *true* richness at redshift $z = 0.2$. The inset shows a section of $P(\lambda^{\mathrm{ob}}|\lambda^{\mathrm{true}})$ for $\lambda^{\mathrm{true}} = 25$ (*dashed* line in the main plot). Note the non-Gaussian tail to high richness due to projection effects, and the low-richness tail due to percolation effects.

accuracy and precision of this formalism, and combined it with numerical simulations to calibrate the impact of projection effects and observational noise in the SDSS DR8 redMaPPer catalogue. Here, we provide a succinct summary of the conclusions from that work, and refer the reader to Costanzi et al. (2018) for details.

The background subtraction and photometric noise terms are Gaussian, and characterized through random injection of synthetic clusters into the data. Projection and percolation are characterized through the use of numerical simulations. The projection noise is characterized as an exponential, and the percolation noise is modelled through partial masking of a cluster richness.

Fig. 2 shows the distribution $P(\lambda^{\mathrm{ob}}|\lambda^{\mathrm{true}})$ as a function of λ^{true} at redshift $z = 0.2$. The inset shows a cross-section of the distribution for $\lambda^{\mathrm{true}} = 25$. The three main components of the distribution are obvious by eye: a Gaussian kernel due to observational noise, a large tail to high richness due to projection effects, and a low-richness tail due to percolation effects.

We note that the calibration of $P(\lambda^{\mathrm{ob}}|\lambda^{\mathrm{true}})$ depends on the input cosmology and richness–mass relation parameters adopted to generate the synthetic cluster catalogue. However, we verified in Costanzi et al. (2018) that this assumption has no impact on the posterior of the cosmological parameters. In Section 6, we explicitly test the robustness of our cosmological constraints to different calibrations of $P(\lambda^{\mathrm{ob}}|\lambda^{\mathrm{true}})$.

3.2 Mass function systematics

The modelling of the cluster counts and mean cluster masses depends on the halo mass function. Here, we use the Tinker et al. (2008) halo mass function. Tinker et al. (2008) report their mass function formula to be accurate at the ≈ 5 per cent level, but we do not have a robust estimate of the associated systematic uncertainty as a function of mass. Moreover, a number of studies comparing different halo finders and fitting functions suggest a systematic uncertainty of the order of 10 per cent (e.g. Knebe et al. 2013; Hoffmann, Bel & Gaztañaga 2015; Despali et al. 2016). To characterize the systematic uncertainty in the halo mass function in dark matter only simulations we introduce two nuisance parameters q and s relating the Tinker et al. (2008) mass function to the true mass function via

$$n(M, z) = n(M, z)^{\mathrm{Tinker}}\left(s\log(M/M^*) + q\right),\tag{10}$$

where the pivot mass is set to $\log(M^*) = 13.8\,h^{-1}\,M_\odot$. Note that if $q = 1$ and $s = 0$, then the halo mass function is given by the Tinker et al. (2008) formula.

We set the priors on q and s using the ensemble of simulations developed as part of the Aemulus project (DeRose et al. 2019). This is a set of 40 N-body simulations spanning a range of cosmologies in the redshift range $0.0 < z < 1.0$. Each simulation box has a length $L = 1050\,h^{-1}$ Mpc and contains 1400^3 particles. The particle mass is cosmology dependent, and averages $\approx 3.5 \times 10^{10}\,h^{-1}\,M_\odot$. The cosmologies sampled by the simulation spans the 4σ confidence interval from WMAP (Hinshaw et al. 2013) and *Planck* (Planck Collaboration XIII 2016a) in combination with BAO data (Anderson et al. 2014) and the Union 2.1 Super-Nova (SN) data (Suzuki et al. 2012). Halo catalogues were generated using the ROCKSTAR algorithm (Behroozi et al. 2013). Further details of the simulation data as well as the convergence tests done to ensure the reliability of these simulations are presented in DeRose et al. (2019).

We fit the simulation halo abundance data for the nuisance parameters s and q at each snapshot of each of the 40 simulations by computing the ratio $n^{\text{Sims}}(M, z)/n(M, z)^{\text{Tinker}}$. Next, we model the distribution of (s, q) values as Gaussian, and fit for the mean values and covariance matrix describing the scatter of (s, q) across all 320 snapshots. We find $\bar{s} = 0.037$ and $\bar{q} = 1.008$, with a covariance matrix:

$$\mathrm{C}(\bar{s}, \bar{q}) = \begin{bmatrix} 0.00019 & 0.00024 \\ 0.00024 & 0.00038 \end{bmatrix}. \tag{11}$$

The above matrix accounts for both statistical uncertainties in the recovered s and q means, and fluctuations in s and q across simulations. The variance of q corresponds to a 6 per cent uncertainty in the amplitude of the halo mass function, consistent with the quoted precision in Tinker et al. (2008). The above covariance matrix and best-fitting values define the bivariate Gaussian priors for s and q in our cosmological analysis. Future analyses will benefit from the significantly higher precision that can be achieved using emulators (e.g. McClintock et al. 2019b).

The above analysis does *not* account for the impact of baryons on the halo mass function. Several recent works have estimated the impact of baryonic feedback on total masses of haloes and, thereby, the mass function (e.g. Cui, Borgani & Murante 2014; Velliscig et al. 2014; Bocquet et al. 2016; Springel et al. 2017). These works all find that baryonic impact decreases with increasing radial aperture. For the specific mass definition we adopt, namely a 200 overdensity criterion relative to mean, the impact of AGN-based full physics is modest for massive ($M \gtrsim 10^{14}\,h^{-1}\,M_\odot$) haloes. In the IllustrisTNG simulation, full physics leads to a mean enhancement of ~ 3 per cent while multiple methods analysed by Cui et al. (2014) produce mainly decrements in M_{200c} of roughly similar magnitude. Due to the current uncertainty in modelling baryonic effects, we defer its inclusion into the error budget of the halo mass function to future work. For now, we simply note that a 3 per cent systematic uncertainty in the halo mass function is already subdominant to the precision of the Tinker mass function, as characterized by our model parameters s and q.

3.3 Covariance matrix

Having specified the expectation values for our observables (cf. Section 3.1) we need to define the covariance matrix of our data vector in order to fully specify the likelihood function. Here, we assume that the abundance and weak lensing data are uncorrelated.

This assumption is well justified: the weak lensing error budget is strongly dominated by shape noise, and the dominant systematic is the overall multiplicative shear and photo-z bias of the source catalogue. None of these errors affect the abundance data, so the two are clearly uncorrelated.

Our Gaussian likelihood model takes the form

$$\mathcal{L}(\boldsymbol{d}|\boldsymbol{\theta}) \propto \frac{\exp\left[-\frac{1}{2}(\boldsymbol{d} - \boldsymbol{m}(\boldsymbol{\theta}))^T\,\boldsymbol{C}^{-1}\,(\boldsymbol{d} - \boldsymbol{m}(\boldsymbol{\theta}))\right]}{\sqrt{(2\pi)^M\det(\boldsymbol{C})}}. \tag{12}$$

where $\boldsymbol{C}$ is the total covariance matrix detailed below, and $\boldsymbol{d}$ and $\boldsymbol{m}(\boldsymbol{\theta})$ are, respectively, the data vectors (see Table 1) and the expectation values for the number counts and $\log M$ (equations 2 and 5, respectively).

In reality, the likelihood for the abundance data is a convolution of a Poisson error on the counts and a Gaussian error due to density fluctuations within the survey area (e.g. Hu & Cohn 2006; Takada & Spergel 2014). Such a convolution does not have an analytic closed form. Here, we take care to ensure that all of our richness bins are well populated – our least populated richness bin contains over 200 galaxy clusters – so that the Poisson component can be adequately modelled with a Gaussian distribution. Consequently, our likelihood for the abundance data can be modelled as a Gaussian with a total covariance matrix having three distinct contributions:

(i) A Poisson contribution due to the Poisson fluctuation in the number of haloes at given mass in the survey volume.

(ii) A sample variance contribution due to the fluctuations of the density field in the survey volume.

(iii) A contribution due to uncertainty in the miscentring corrections detailed in Section 2.2.

The Poisson and sample variance contributions to the covariance matrix are computed analytically at each step of the chain to properly account for their dependence on cosmology and model parameters. At high richness, the Poisson contribution dominates, with sample variance becoming increasingly important at low richness (Hu & Kravtsov 2003). The analytical expression used to derive these two terms is provided in Appendix A, and it is validated by comparing it to Jackknife estimates of the same derived from simulated catalogues (see Fig. 3).

Turning to the uncertainty in the weak lensing mass estimates, we use the posteriors from the stacked weak lensing analysis described in Section 2.3 (see Table 1). These posteriors are found to be nearly Gaussian in the log. The errors include not just the statistical uncertainty of the measurement, but also systematic uncertainties due to shear and photo-z biases (multiplicative shear bias), cluster projections, halo triaxiality, and miscentring effects. The overall shear and photo-z multiplicative bias is shared across all richness bins, so this systematic is modelled as being perfectly correlated across bins. The mass error in each bin associated with the multiplicative bias is estimated as in Melchior et al. (2017, section 5.7) and McClintock et al. (2019b, section 5.6).

In summary, our likelihood:

(i) Is Gaussian in the abundances, and includes Poisson, sample variance, and miscentring uncertainties.

(ii) Is lognormal in the weak lensing masses, as per the posteriors of Simet et al. (2017). It also accounts for the covariance due to shared multiplicative shear and photo-z biases, blended sources, and cluster triaxiality and projection effects. These systematics are assumed to be perfectly correlated across all richness bins.

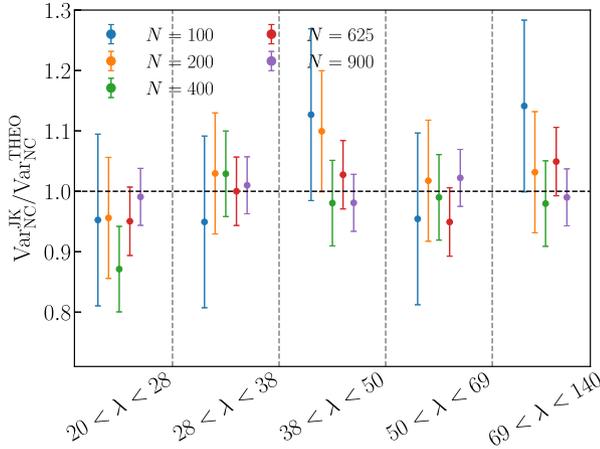(iii) Has no covariance between the abundance and weak lensing data. We expect this to be an excellent approximation.

Figure 3. Comparison between the analytically derived variance for the number counts and the one derived from the mock catalogue. Different colours correspond to the different number of patches used to estimate the Jackknife covariance matrix. Error bars are estimated from the jackknife covariance matrices itself assuming the jackknife realizations to be Gaussian distributed.

The posteriors from our analysis are fully marginalized over all sources of systematic uncertainty described above.

4 VALIDATION TESTS

We validate our likelihood framework by placing cosmological constraints from a synthetic cluster catalogue whose cosmology and richness–mass relation is known a priori. The mock data are generated starting from an *N*-body simulation run with 1400^3 dark matter particles in a box of comoving size $L = 1050 \, \mathrm{Mpc} \, h^{-1}$. The code used is L-GADGET, a variant of GADGET (Springel 2005). The simulation assumes a flat-Λ cold dark matter (ΛCDM) model with $\Omega_m = 0.286$, $h = 0.7$, $\Omega_b = 0.047$, $n_s = 0.96$, and $\sigma_8 = 0.82$. Light-cone data, including a halo catalogue down to $M_{200m} = 10^{12.5} h^{-1} \mathrm{M}_\odot$, is constructed from the simulation on the fly. The halo finder is `rockstar` (Behroozi et al. 2013). For further details, see DeRose et al. (2019); this is one realization of the L1 box described in that work.

We build a synthetic cluster catalogue as follows. First, each halo is assigned a richness λ^{true} drawn from the $P(\lambda^{\mathrm{true}}|M, z)$ distribution detailed in Section 3.1. We set our fiducial model parameters to: $\alpha = 0.704$, $\log M_{\min} = 11.0$, $\log M_1 = 12.12$, and $\sigma_{\ln \lambda} = 0.25$. These fiducial values have been chosen by inverting the mass–richness relation of Simet et al. (2017). The assigned richnesses are then modified to account for observational noise plus projection effects as described in Costanzi et al. (2018, see their section 3.2).

Given this synthetic cluster catalogue, we compute our observable data vectors. The cluster counts are measured using the same binning scheme as for the real data (see Table 1). The synthetic weak lensing masses are set to the mean halo mass in each richness bin. We also add a lognormal noise to the mean weak lensing masses by drawing from the covariance matrix described in Section 3.3. To mimic the fact that the weak lensing masses are estimated assuming $\Omega_m = 0.3$ while the simulation use the fiducial value $\Omega_m = 0.286$, we invert equation (1) to arrive to our final mock data vector:

$$\log \bar{M}^{\mathrm{WLMOCK}} = \log \bar{M}^{\mathrm{WL}} \big|_{\Omega_m = 0.286} - \left(\frac{\mathrm{d} \log M^{\mathrm{WL}}}{\mathrm{d}\Omega_m} \right) (0.286 - 0.3).$$

Fig. 4 shows the constraints obtained by analysing a realization of our synthetic data set with our pipeline. This analysis varies the same parameters and assumes the same priors as the real data analysis (see Section 6). It successfully recovers the true values of the parameters of our synthetic data set (*red* lines in the triangle plots). Because this test relied on a single simulation, we could not use it to validate the width of our posteriors.

5 BLINDING AND UNBLINDING

In order to avoid confirmation biases our cosmological analysis was performed blinded. By 'blinded', we mean that the following protocols were followed:

(i) The cosmological parameters in the MCMC were randomly displaced before being stored, and the random displacement was stored in binary (i.e. a not-human-readable format).

(ii) All modelling choices – specifically which set of cosmological models and models for the scaling relations we would consider – were made before unblinding. In this work, we chose to focus exclusively on flat ΛCDM cosmologies with massive neutrinos. Our choice to let neutrino mass vary follows the practice of the DES Year 1 combined probe analysis (DES Collaboration 2018).

(iii) The set of scaling relation models considered in our analysis was fully specified before unblinding. These are detailed in Section 6.2.

(iv) All priors were set before unblinding

(v) The metrics for consistency with external data sets were selected before unblinding. Here, we distinguish between data sets with which we intend to combine our analysis and other large-scale-structure data sets that constrain the $S_8 \equiv \sigma_8 (\Omega_m / 0.3)^{1/2}$ parameter. For the latter, we consider analyses *A* and *B* to be consistent if their central values of S_8 deviate by no more than $3\sigma_{\mathrm{tot}}$, where $\sigma_{\mathrm{tot}}^2 = \sigma_A^2 + \sigma_B^2$. For the former, consistency between two data sets *A* and *B* was established by testing whether the hypothesis $\boldsymbol{p}_A - \boldsymbol{p}_B = 0$ is acceptable (see method '3' in Charnock, Battye & Moss 2017). Here, $\boldsymbol{p}_A$ and $\boldsymbol{p}_B$ are the model parameters of interest as constrained by data sets *A* and *B*, respectively. The two data sets were deemed to be consistent if the point $\boldsymbol{p}_A - \boldsymbol{p}_B = 0$ falls within the 99 per cent confidence level of the multidimensional distribution of $\boldsymbol{p}_A - \boldsymbol{p}_B$. If two data sets were found to be inconsistent with one another, we did not consider the combined analysis. We note that in order for this test to be the sharpest possible test, it is important to restrict one-self to parameter sub-spaces that are well constrained in both data sets. To that end, in all cases we restrict the parameter space for comparison to the set of parameters whose posterior is at most half as uncertain as the prior of each individual data set.

(vi) No comparison of our cosmological constraints to any other data sets were performed prior to unblinding.

The weak lensing analysis upon which our work relies was not performed blind (Simet et al. 2017), though our forthcoming analysis using data from the DES data will have benefited from a blind weak lensing analysis. Importantly, all relevant weak lensing priors – specifically the multiplicative shear bias, photometric redshift correction, source dilution, etc – were finalized well before the advent of our particular analysis: no tuning of any input catalogue was done in response to the weak lensing analysis of Simet et al. (2017) or our own cosmological analysis. Finally, we note that while some people in our team were involved with the cosmological analysis of the maxBCG clusters catalogue, the development of redMaPPer was *not* based on inferences from maxBCG clusters, so no prior information was 'baked in' into the construction of the catalogue.
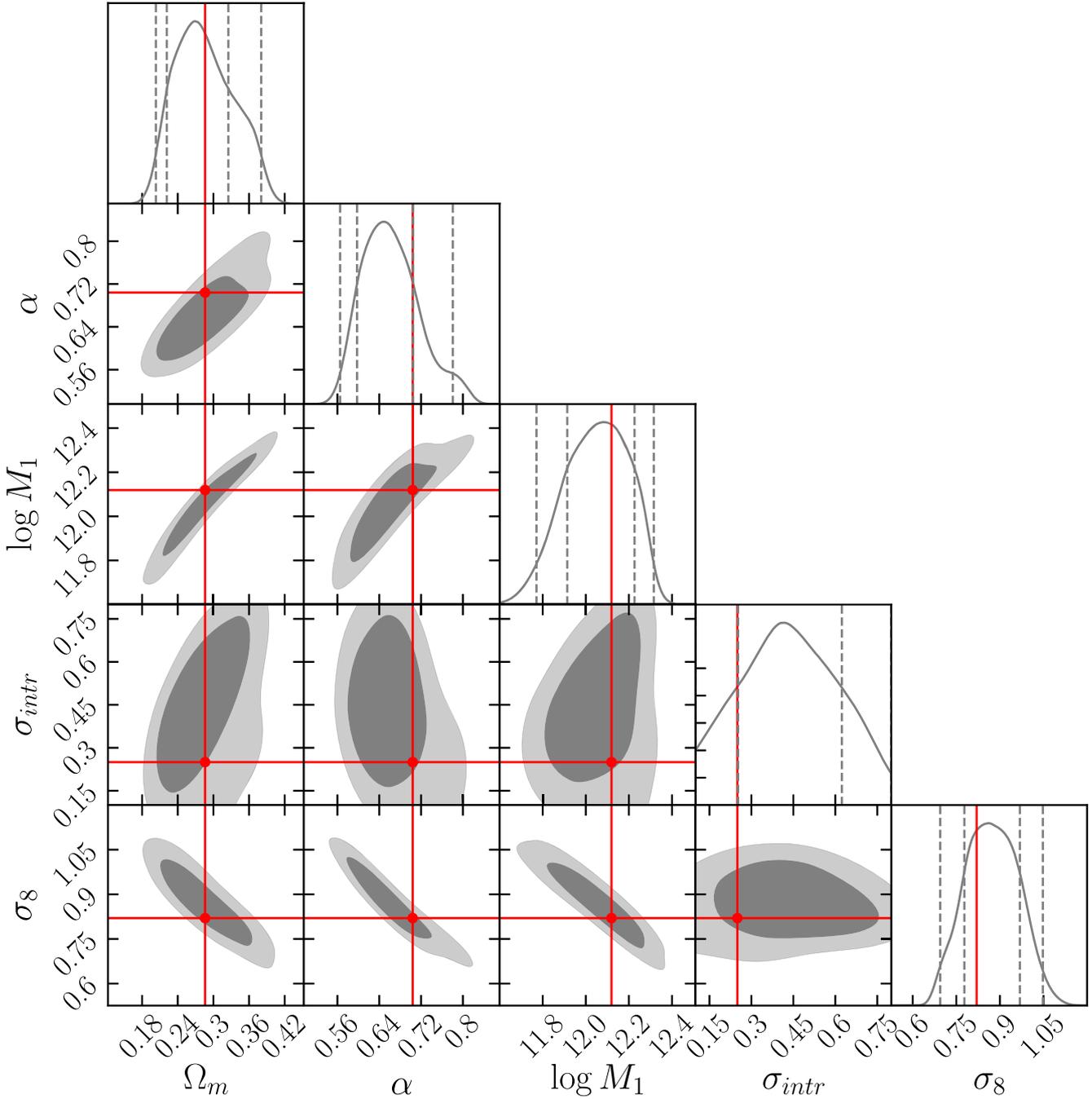
Figure 4. 68 per cent and 95 per cent confidence contours obtained running our pipeline on mock data. The input parameter values used to generate the simulation and the mock data catalogue are shown in *red*. The *dashed* lines shown in the 1D marginalized distributions (diagonal of the triangle plot) correspond to the 0.025, 0.16, 0.84, and 0.975 quantiles of the distributions. Not included in this plot is the parameter $M_{\min}$, which is prior dominated.

Our unblinding protocol was defined by the set of requirements detailed below.

(i) Our inference pipeline had to successfully recover the input cosmology in a synthetic data set. For details, see Section 4.

(ii) All SDSS-only chains (including alternative models) were run demanding the fulfilment of the Gelman–Rubin criteria (Gelman & Rubin 1992) with $R - 1 \leq 0.03$ being our convergence criteria.

(iii) We had to demonstrate systematics uncertainties in our model for $P(\lambda^{\mathrm{ob}}|\lambda^{\mathrm{true}}, z)$ did not appreciably bias our cosmological

posteriors. To this end we run our analysis using an extreme model for $P(\lambda^{\mathrm{ob}}|\lambda^{\mathrm{true}}, z)$ that neglect the contribution from correlated structures to the observed richness (random-point-injection model, see Section 6.2). We adopted half of the systematic shift in the values of the cosmological parameters between our fiducial model and this extreme model as our estimate of the associated systematic uncertainty. Note this definition implies that the extreme random-point-injection model is consistent with our fiducial model at 2σ despite being clearly extreme. We demanded that these systematic shifts be less than the corresponding statistical uncertainties.

(iv) We explicitly verified that the priors of all parameters that we expected would be well-constrained a priori are not informative, that is the posteriors of such parameters did not run into the priors within the 95 per cent confidence region. In case this condition was not fulfilled we planned to extend the relevant prior ranges until the requirement was met. Parameters that are prior dominated (i.e. their posterior runs into the prior) are $M_{\min}$, σ_{intr}, s, q, h, $\Omega_{\text{b}}h^2$, $\Omega_\nu h^2$, and n_{s}. All of these were expected to be prior dominated a priori, and all prior ranges were purposely conservative. Of these, the two that might be most surprising to the reader are $M_{\min}$ and σ_{intr}, as these parameters help govern the richness–mass relation. However, notice that $M_{\min}$ is the mass at which haloes begin to host a single central galaxy; since our cluster sample is defined with the richness threshold $\lambda \geq 20$, the mass regime of haloes that host a single galaxy is not probed by our data set. Likewise, our data vector is comprised only of the mean mass of galaxy clusters in a given richness bin, a quantity that is essentially independent of the scatter in the richness–mass relation (see McClintock et al. 2019a).

(v) The χ^2 of the data for our best-fitting model must be acceptable. To this end we considered the best-fitting χ^2 distribution recovered from 100 mock data realizations generated from the best-fitting model of the data. We assumed these 100 trials were distributed according to a χ^2 distribution, and fit for the effective number of degrees of freedom. The number of degrees of freedom is not obvious a priori due to the presence of priors in the analysis. We considered the χ^2 of our data to be not acceptable if the probability to exceed the observed value was less than 1 per cent, after marginalization over the posterior for the effective number of degrees of freedom. We emphasize that verifying an acceptable χ^2 does not unblind the cosmological parameters. While our model did indeed have an acceptable χ^2 (see Section 6.1 for details), our plan was to revisit our model and covariance matrix estimation procedures in the case of an unacceptable χ^2 value. This proved unnecessary.

(vi) Finally, this paper underwent internal review by the collaboration prior to unblinding. All members of the DES cluster working group, as well as all internal reviewers, agreed that our analysis was ready to unblind before we proceeded.

No changes to the analyses were made post-unblinding. Work performed as part of the DES Y1 cluster cosmology analysis has demonstrated that the selection effects corrections applied here were smaller than those observed in simulations. Details will be presented in that paper (DES collaboration, in preparation). Updated SDSS constraints will be presented in a forthcoming work (Kirby et al., in preparation) that further adds multiwavelength data to the analysis. In the absence of the additional multiwavelength data, we expect these additional corrections will result in only minor (less than 1σ) changes in the posteriors.

6 RESULTS

6.1 SDSS cluster abundances and weak lensing data

We model the abundance of galaxy clusters and their weak lensing masses assuming a flat ΛCDM cosmological model, allowing for massive neutrinos. The full set of cosmological parameters we consider is: $\ln(10^{10}A_{\text{s}})$, Ω_{m}, n_{s}, $\Omega_{\text{b}}h^2$, h, and $\Omega_\nu h^2$. Neutrinos are included assuming three degenerate neutrino species. We adopt the same priors as in the DES Year 1 analysis of galaxy clustering and weak lensing (DES Collaboration 2018), with the exception of h, where we adopt the slightly more restrictive prior $h = 0.7 \pm 0.1$.

There are also two parameters (s and q) associated with systematic uncertainties in the halo mass function, and 4 parameters governing the richness–mass relation : $M_{\min}$, M_1, α, and σ_{intr}. The priors for all parameters are summarized in Table 3. We have explicitly verified that increasing the range of the priors adopted for the richness–mass relation parameters does not adversely impact the recovered cosmological constraints.

The result of our MCMC fitting procedure is shown in Fig. 5, while the marginalized posterior values are reported in Table 3. Parameters not shown in Fig. 5 and without a quoted posterior in Table 3 are those whose posterior is equal to their prior. Also shown in the table is the posterior for the so-called cluster normalization condition parameter $S_8 \equiv \sigma_8(\Omega_{\text{m}}/0.3)^{0.5}$. In practice, the σ_8–Ω_{m} degeneracy in our cosmology analysis corresponds to

$$\sigma_8 \left(\frac{\Omega_{\text{m}}}{0.3} \right)^{0.47} = 0.80 \pm 0.04. \tag{13}$$

Nevertheless, unless otherwise specified in the text, from this point on we will focus on the cluster normalization condition $S_8 \equiv \sigma_8(\Omega_{\text{m}}/0.3)^{0.5}$ as it has become a standard parameter in the literature.

A comparison of our best-fitting model with the data is shown in Fig. 1. The χ^2 of our best-fitting model is $\chi^2 = 5.71$. To assess the goodness of the fit we generated 100 mock data vectors from our best-fitting model of the data and, for each of them, we recovered the best-fitting χ^2 value. Assuming a χ^2 distribution for the 100 trials we fit for the effective number of degree of freedom, finding $\nu_{\text{eff}} = 7.56 \pm 0.37$ (see Fig. 6). This corresponds to a probability to exceed of $p = 0.64 \pm 0.04$, thus the model provides an acceptable description of the data.

We wish to determine whether the error budget in the cosmological parameter S_8 is dominated by uncertainties in the abundance data or the weak lensing data. To do so, we first compute the predicted abundance and weak lensing data using our best-fitting model. We then run two additional chains using the predicted expectation values as a synthetic data vector. The key difference between the two chains is that for one we reduce the abundance covariance matrix by a factor of 100, while for the other chain we reduce the covariance matrix of the weak lensing data by a factor of 100. By comparing the cosmological posteriors for these two chains we can determine if there is one observable that dominates our error budget. In both cases the corresponding posterior on S_8 have an error bar $\sigma_{S_8} = 0.03$ (see *left-hand* panels of Fig. 7), demonstrating that both observables contribute in comparable ways to the total error budget of S_8.

The balance between weak lensing errors and abundance uncertainties is surprising in light of the fact that all analyses to date have been dominated by uncertainties in the calibration of the mean of the observable–mass relation. Nevertheless, this feature of our results can be easily understood. The left-hand panel of Fig. 7 demonstrates that there is a strong degeneracy between S_8 and σ_{intr}. Unlike previous analysis, which have incorporated well-motivated simulation-based priors on the scatter of the observable–mass relation, our analysis adopts a very broad prior on the scatter of the richness–mass relation. This broad prior reflects the difficulty inherent to predicting properties of the richness–mass relation a priori. Since the scatter parameter impacts the detailed shape of the abundance function – larger scatter leads to flatter abundance functions – exquisitely precise measurements of the abundance function can break the degeneracy between scatter and S_8, leading to significant improvements in the S_8 constraints. Conversely, even modest constraints of the scatter parameter σ_{intr} can break the S_8–σ_{intr} degeneracy, leading to tighter constraints.

Table 3 Model parameters and parameter constraints from the joint analysis of redMaPPer SDSS cluster abundance and weak lensing mass estimates. In the fourth column, we report our model priors: a range indicates a top-hat prior, while $\mathcal{N}(\mu, \sigma)$ stands for a Gaussian prior with mean μ and variance σ^2. In the fifth column are listed the maximum likelihood values of the 1D marginalized posterior along with the 1σ errors. Parameters without a quoted value are those having marginalized posterior distribution corresponding to their prior. Note that systematic uncertainties in the lensing masses are contained in their covariance, and are therefore not explicitly modelled in the likelihood. For the priors on the nuisance parameters s and q we report here only the square root of the diagonal terms of the covariance matrix defined in equation (11). The distribution characterizing the impact of observational noise, projection effects, and percolation includes several additional parameters that are held fixed. The systematic uncertainty associated with uncertainties in these parameters is estimated by repeating our analysis using an extreme set of values for these parameters, as estimated using random clusters in the SDSS (Costanzi et al. 2018). Because these parameters are not marginalized over in our chains, they are not included in this table. We stress that the impact of the associated systematic error is negligible relative to the recovered width of our cosmological posteriors.

Parameter	Description	Prior	Posterior
Ω_m	Mean matter density	$[0.0, 1.0]$	$0.22^{+0.05}_{-0.04}$
$\ln(10^{10}A_s)$	Amplitude of the primordial curvature perturbations	$[-3.0, 7.0]$	$3.97^{+0.67}_{-0.47}$
σ_8	Amplitude of the matter power spectrum	$-$	$0.91^{+0.11}_{-0.10}$
$S_8 = \sigma_8(\Omega_m/0.3)^{0.5}$	Cluster normalization condition	$-$	$0.79^{+0.05}_{-0.04}$
$\log M_{\min}$ [$M_\odot \, h^{-1}$]	Minimum halo mass to form a central galaxy	$(10.0, 14.0)$	11.2 ± 0.2
$\log M_1$ [$M_\odot \, h^{-1}$]	Characteristic halo mass to acquire one satellite galaxy	$\log(M_1/M_{\min}) \in [\log(10), \log(30)]$	$12.42^{+0.16}_{-0.13}$
α	Power-law index of the richness–mass relation	$[0.4, 1.2]$	$0.65^{+0.05}_{-0.07}$
$\sigma_{\rm intr}$	Intrinsic scatter of the richness–mass relation	$[0.1, 0.8]$	<0.4
s	Slope correction to the halo mass function	$\mathcal{N}(0.037, 0.014)$	$-$
q	Amplitude correction to the halo mass function	$\mathcal{N}(1.008, 0.019)$	$-$
h	Hubble rate	$\mathcal{N}(0.7, 0.1)$	$-$
$\Omega_b h^2$	Baryon density	$\mathcal{N}(0.02208, 0.00052)$	$-$
$\Omega_\nu h^2$	Energy density in massive neutrinos	$[0.0006, 0.01]$	$-$
n_s	Spectral index	$[0.87, 1.07]$	$-$

We demonstrate the impact that a modestly precise prior can have on our cosmological posteriors by redoing our analysis while imposing a flat prior $\sigma_{\rm intr} \in [0.1: 0.3]$. The corresponding posterior for S_8 is $S_8 = 0.77 \pm 0.03$. If we now repeat our sensitivity analysis, and shrink the weak lensing mass errors, the width of the S_8 posterior decreases to $\sigma_{S_8} = 0.01$, while decreasing the abundance errors while holding the weak lensing errors fixed has a negligible impact on the posterior. These trends are illustrated in the right-hand panel of Fig. 7. Evidently, external constraints on the scatter of the richness–mass relation of redMaPPer clusters are extremely valuable from a cosmological perspective.

6.2 Robustness to assumptions about the richness–mass relation

Fig. 5 shows that there is strong covariance between cosmological parameters and parameters governing the richness–mass relation. Consequently, one may ask to what extent are our cosmological constraints sensitive to the detailed assumptions we have made about the richness–mass relation. To address this question, we have repeated our analysis with a range of richness–mass relation models as summarized in Fig. 8. The models considered are as follows:

(i) A model that allows for the intrinsic scatter $\sigma_{\rm intr}$ to vary with mass via

$$\sigma_{\rm intr}(M) = \sigma_{\rm intr,0}(M/(M_1 - M_{\min}))^\beta. \tag{14}$$

(ii) A model that neglects the perturbations on the observed richness due to correlated structures. To this end we set $P(\lambda^{\rm ob}|\lambda^{\rm true}, z^{\rm true})$ equal to the probability distributions recovered from injecting synthetic clusters at random positions in the survey mask. This calibration provides a very strict lower limit on the scatter of $\lambda^{\rm ob}$ due to projection effects: clusters do contain correlated large-scale structure. The difference in the posteriors of the cosmological

parameters between our fiducial run and the random-point-injection model places a strict upper limit on the systematic associated with our modelling of projection effects.

(iii) A model in which the richness–mass relation is a simple power law – $\langle \lambda^{\rm true}|M\rangle = \lambda_0(M/10^{14.344})^\alpha$ – and $P(\lambda^{\rm true}|M)$ is a lognormal distribution in which the total scatter it the sum of a Poisson-like term and an intrinsic scatter term – $\sigma^2_{\ln \lambda^{\rm true}} = \sigma^2_{\rm intr} + (\langle \lambda^{\rm true}|M\rangle - 1)/\langle \lambda^{\rm true}|M\rangle^2$.

(iv) The richness–mass relation model of Murata et al. (2018). This model assumes $P(\lambda^{\rm ob}|M)$ is lognormal, the mean richness–mass relation is a power law, and the intrinsic scatter is mass-dependent, and given by $\sigma_{\rm intr}(M) = \sigma_{\rm intr,0} + \beta \ln(M/2.2 \times 10^{14})$. According to Murata et al. (2018) all integrals are truncated at $M_{\min} = 10^{12} \, h^{-1} \, M_\odot$. Reassuringly, when we mirror the analysis of Murata et al. (2018) and fix our cosmological parameters to Planck Collaboration XIII (2016a) we reproduce their results despite significant methodological differences in how the weak lensing data is incorporated into the likelihood.

As can been seen in Fig. 8 our cosmological posteriors are all consistent with one another. It is clear that the more restrictive parametrizations (e.g. lognormal + power-law) result in somewhat tighter constraints. Notably, our standard result – which we believe is the most appropriate model – results in the most conservative posteriors. In particular, we see that opening up the freedom of a mass-dependent intrinsic scatter does not negatively impact the posterior on S_8. We also note that our random-point-injection model, which grossly underestimates the impact of projection effects, had a small impact on the posterior of the intrinsic scatter, modifying instead the best-fitting value for the slope of the richness–mass relation, a degeneracy that should be easily broken via multiwavelength analyses of the redMaPPer clusters. Finally, we note that the Murata-like parametrization has the largest impact on our posteriors, with the systematic shift in S_8 being comparable to the width of
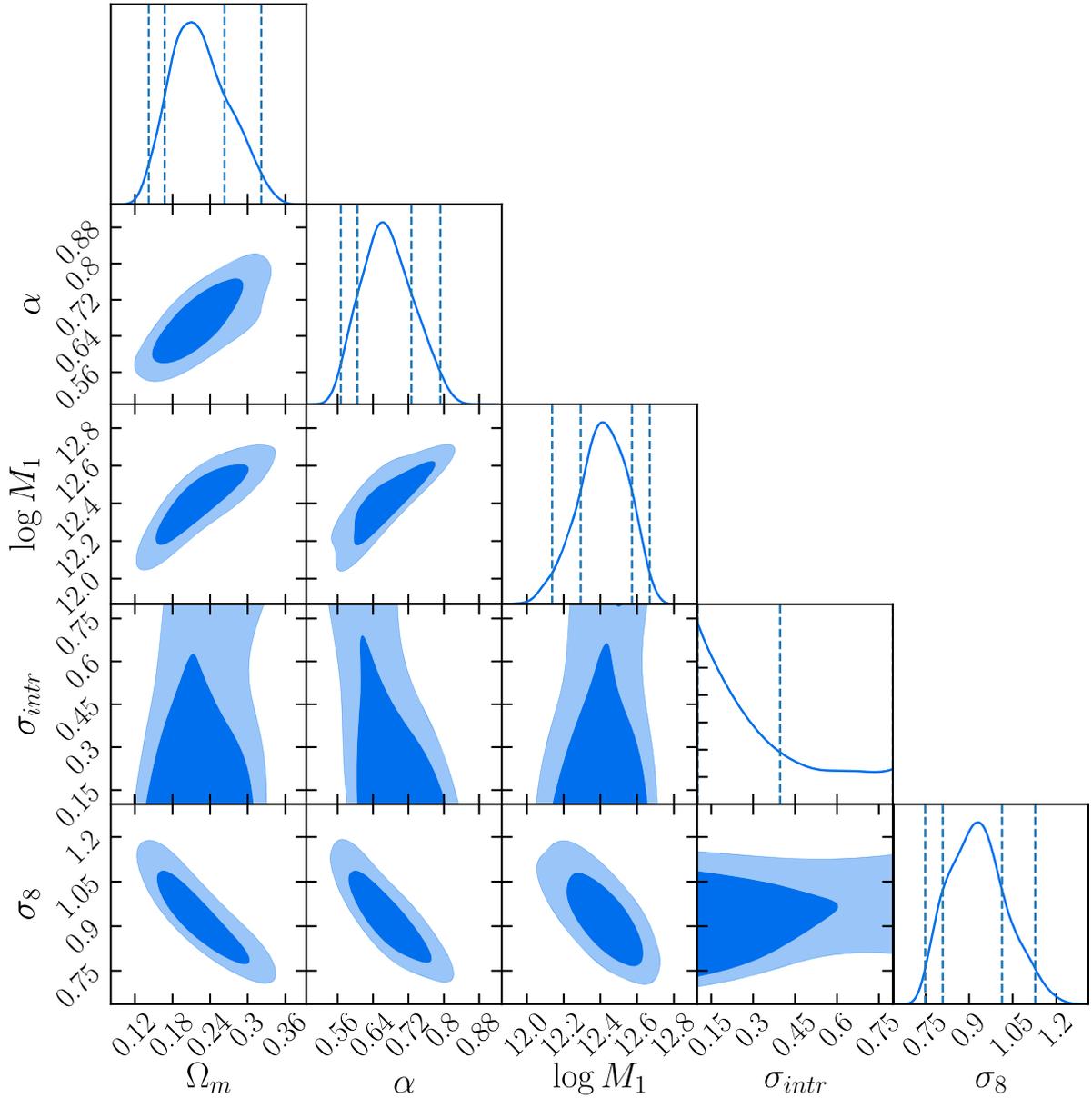
Figure 5. Marginalized posterior distributions of the fitted parameter. The 2D contours correspond to the 68 per cent and 95 per cent confidence levels of the marginalized posterior distribution. The dashed lines on the diagonal plots correspond, respectively, to the 2.5th, 16th, 84th, and 97.5th percentile of the 1D posterior distributions. The description of the model parameters along with their posterior are listed in Table 1. Not included in this plot is the parameter M_{min}, which is prior dominated.

the posterior. We will address the origin of this shift in the next section.

6.3 The observable–mass relation for redMaPPer clusters

The left-hand panel of Fig. 9 shows the observed richness–mass relation $\langle \lambda^{ob}|M \rangle$ for our fiducial model at the mean sample redshift $z = 0.22$. The error bars reflect the posterior of the mean relation at each mass. These are computed as follows: for each point in our chains we evaluate $\langle \lambda^{ob}|M \rangle$ along a grid of masses. The mean and variance of $\langle \lambda^{ob}|M \rangle$ across the chain are then recorded. In the left-hand panel of Fig. 9, we use these quantities to plot the 68 per cent confidence interval for the posterior of the mean of the richness–mass relation. The central panel of Fig. 9 is computed in a

similar way, only now we show the posterior for the scatter $\mathrm{Var}^{1/2}$ $(\lambda^{ob}|M)$.[8]

[8] A reader might find useful to have simple power-law fits to the data shown in Fig. 9. We provide such fits below:

$$\langle \lambda^{ob}|M \rangle = 30.0 \left(\frac{M}{3 \times 10^{14} \, [\mathrm{M}_\odot h^{-1}]} \right)^{0.75}$$

$$\mathrm{Var}^{1/2}(\lambda^{ob}|M) = 14.7 \left(\frac{M}{3 \times 10^{14} \, [\mathrm{M}_\odot h^{-1}]} \right)^{0.54}.$$

The fits correspond to the best-fitting relations. No errors are provided since these are meant to be 'quick-look' references. Detailed quantitative analyses should rely on the full posterior of our model, which will be made available at http://risa.stanford.edu/redmapper/ when the paper is published.
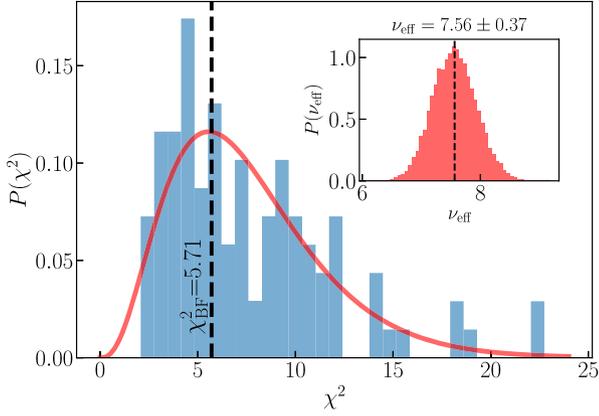
Figure 6. Goodness of fit analysis. The *blue* histogram shows the distribution of the best-fitting χ^2 values recovered from 100 mock data realizations generated from the best-fitting model of the data. The *red* histogram in the inset plot shows the posterior distribution for the effective number of degrees of freedom obtained by fitting a χ^2 distribution to the above 100 χ^2 values. The *red solid* line represents the χ^2 distribution for the best-fitting model ($\nu_{\rm eff} = 7.56$), while the vertical *dashed* line corresponds to the χ^2 value of the data.

For comparison we include in the two panels the richness–mass relation and scatter derived in Murata et al. (2018), who analysed this sample of clusters using the same weak lensing shear catalogue we employed. There are significant methodological differences between the two analyses. Specifically, Murata et al. (2018)

(i) use emulators instead of an analytic model for the weak lensing profile of clusters, effectively holding the concentration of the galaxy clusters fixed. They also place no priors on the miscentring parameters;

(ii) adopt a lognormal model for $P(\lambda^{\rm ob}|M)$;

(iii) adopt a power-law relation for both the mean and variance of $\lambda^{\rm ob}$ at fixed mass.

Despite methodological differences, the two results are remarkably similar over the mass range probed by the survey ($M \gtrsim 10^{13.5}\,{\rm M}_\odot\,h^{-1}$, see below). It is especially impressive how well the scatter found in Murata et al. (2018) agrees with our finding, confirming their argument that the mass-trend in the scatter of the richness–mass relation they recovered is due to contamination from projection effects.

There is, however, one notable difference between our results and those of Murata et al. (2018). Fig. 7 of Murata et al. (2018) shows that the mass distribution for clusters in the richness bin $\lambda^{\rm ob} \in [20, 30]$ extends to masses as low as $10^{12}\,h^{-1}\,{\rm M}_\odot$, the mass cut imposed in that analysis. Fig. 10 shows the posterior of the mass distribution for clusters in our analysis, as labelled. Unlike Murata et al. (2018), we do not see any evidence for a population of low-mass ($M \leq 10^{13}\,h^{-1}\,{\rm M}_\odot$) clusters. We believe the large number of low-mass haloes in the Murata et al. (2018) analysis is driven by the combination of a lognormal model whose scatter increases with decreasing mass, and a model that ignores the central/satellite dichotomy at low masses. Our model avoids this problem by (1) enforcing the appropriate Poisson limit in the limit of low $\lambda^{\rm true}$ and (2) developing a simulation-based model for projection effects that adequately characterizes non-Gaussian tails in the distribution $P(\lambda^{\rm ob}|\lambda^{\rm true})$.

As an independent check of our conclusions, we estimate the halo masses of individual redMaPPer clusters using the stellar content of the redMaPPer central galaxy. Specifically, we fit the photometric SDSS data using a stellar population synthesis model to derive the stellar mass of each of the assigned redMaPPer central galaxies (Moustakas et al., in preparation). We then use the UniverseMachine algorithm (Behroozi et al. 2018) to determine the relation between the stellar mass of the central galaxy of a halo and the mass of the parent halo. Using the relation between halo mass and the stellar mass of the central galaxy, we can readily assign a mass estimate to each redMaPPer cluster. We find that the stellar mass estimates of 95 per cent of redMaPPer central galaxies correspond to a halo mass of $2 \times 10^{13}\,h^{-1}\,{\rm M}_\odot$ or higher. While the stellar mass to halo mass relation of central galaxies is relatively uncertain, this result disfavours the existence of a significant population of low-mass ($M \leq 10^{13}\,h^{-1}\,{\rm M}_\odot$) redMaPPer clusters, in agreement with our results.

We suspect that the tail of low-mass haloes recovered in the Murata et al. (2018) model is responsible for the $\sim 1\sigma$ shift in S_8 seen in Fig. 8 when adopting a power-law lognormal model for the richness–mass relation (i.e. the Murata-like analysis): the artificial boost in the abundance of low-richness clusters is compensated by a decrease in the predicted halo abundance, which is in turn achieved by lowering the cluster normalization condition.

Finally, the right-hand panel of Fig. 9 shows the mass-selection function of the galaxy clusters selected in our experiment. That is, it shows the probability $P(M, z)$ that a halo of mass M at redshift z is included in the SDSS redMaPPer sample. This probability is given by

$$P(M, z) = \int_{20}^{\infty} {\rm d}\lambda^{\rm ob}\ P(\lambda^{\rm ob}|M, z). \qquad (15)$$

The probability $P(M, z)$ is evaluated at a grid of masses for each point in the chain, and the corresponding mean and uncertainty is calculated. Using linear interpolation over this grid, we find that the mass value for which the detection probability is 1/2 is $\log M = 14.24[{\rm M}_\odot\,h^{-1}]$.

Using our best-fitting cosmological model we can combine the halo mass function with our recovered richness–mass relation to arrive at our best-fitting mass–richness relation. In particular, for each point in the chain we can readily compute $\langle M|\lambda^{\rm ob}\rangle$ along a grid of richnesses, and calculate mean and variance of these quantities at each $\lambda^{\rm ob}$ value as we sample our posterior. We estimated the mean mass at a grid of values, and computed the corresponding covariance matrix, and then fit the data with a power law to arrive at the corresponding mass–richness relation. The resulting mass–richness relation is shown in Fig. 11 along with the relation derived in Simet et al. (2017). The posteriors for the mass–richness relation in our analysis is

$$\langle M|\lambda\rangle = 10^{14.45\pm0.03} \left(\frac{\lambda}{40}\right)^{1.29\pm0.09}, \qquad (16)$$

where we used only $\lambda^{\rm ob} > 20$ data points (*black* dots in the figure) to fit the power-law relation. This is to be compared to the Simet et al. (2017) relation, $\langle M|\lambda\rangle = 10^{14.42\pm0.04}(\lambda/40)^{1.3\pm0.1}$. Note that the exponent 14.42 has been obtained correcting the best-fitting value 14.37 derived in Simet et al. (2017) assuming $\Omega_{\rm m} = 0.30$ via equation (1) using the mean $\Omega_{\rm m}$ value derived in this analysis. Moreover, we expect a small difference in amplitude due to the updates to our multiplicative shear bias model and the redMaPPer centring fraction. All together, these corrections should boost the amplitude of the mass–richness relation by ≈ 6 per cent, in good agreement with our results.
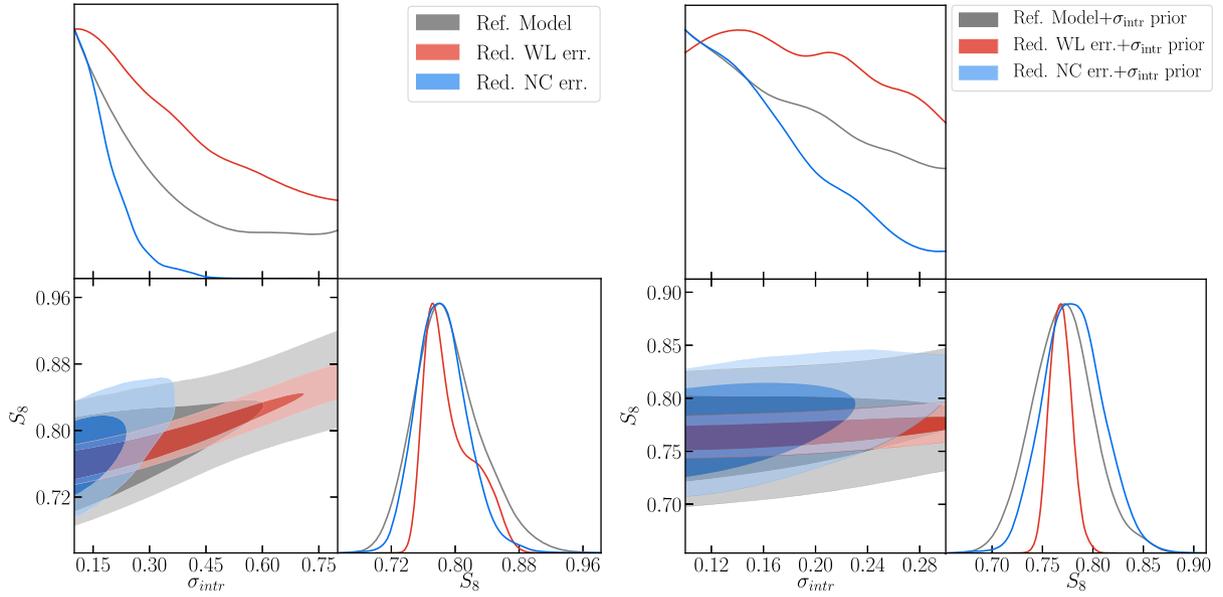
Figure 7. Assessment of the error budget on S_8 associated with our two observables: cluster abundance data and weak lensing mass estimates. *Left-hand* panels: Comparison of the (S_8, $\sigma_{\rm intr}$) constraints derived in our reference model (*grey* contours) and rescaling the weak lensing data (*red* contours) or the number counts (*blue* contours) covariance matrix by a factor 0.01. *Right-hand* panels: Same as the left-hand panels but including a flat prior on the scatter parameter: $\sigma_{\rm intr} \in [0.1: 0.3]$. See the text for additional details and discussion.
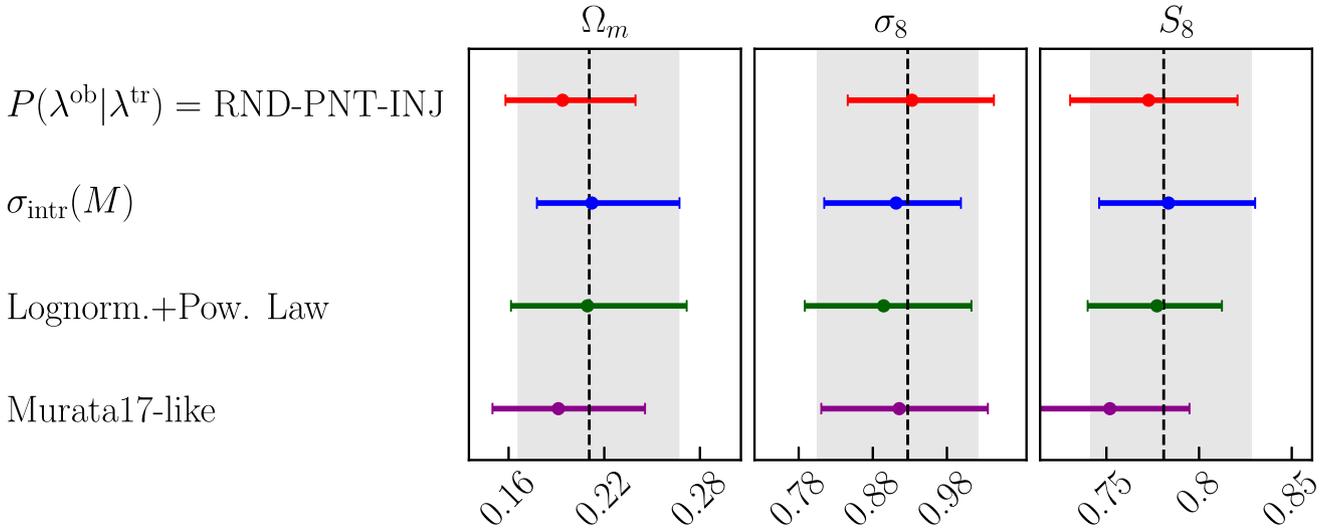
Figure 8. Comparison of the 68 per cent confidence regions for $\Omega_{\rm m}$, σ_8, and S_8 derived assuming different model for $P(\lambda^{\rm ob}|M)$ (see Section 6.2). The shaded area corresponds to the constraints derived using our reference model.

7 COMPARISON TO EXTERNAL DATA SETS

Our analysis allows us to place the constraint $S_8 = 0.79^{+0.05}_{-0.04}$. A comparison of our baseline result (*grey shaded* area) to several other constraints from the literature can be seen in Fig. 12. To estimate the level of tension between two analyses A and B we consider the quantity: $T_{A,B} = |\Delta S_8|/\sigma_{\rm tot}$, where . According to our consistency criterion (see item (v) in Section 5) all the measurements of S_8 from the external data sets we considered are consistent with the one derived in this analysis ($\Delta S_8 < 3\sigma_{\rm tot}$). The most significant difference comes with respect to the cluster constraints from the Atacama Cosmology Telescope cluster sample (Hasselfield et al.

2013), though the significance of this difference is still below $2\sigma_{\rm tot}$. As for the *Planck* DR18 CMB S_8 constraint, the significance of the difference between the two results is only $1.1\sigma_{\rm tot}$.[9]

We planned to combine the SDSS redMaPPer cluster abundances constraints with two distinct external data sets, provided that these data sets were consistent with our results (see item (vii) in Section 5). Namely we considered:

---

[9]The significance of the difference between our S_8 posterior and that of the *Planck* 2015 analysis is $1.2\sigma_{\rm tot}$.
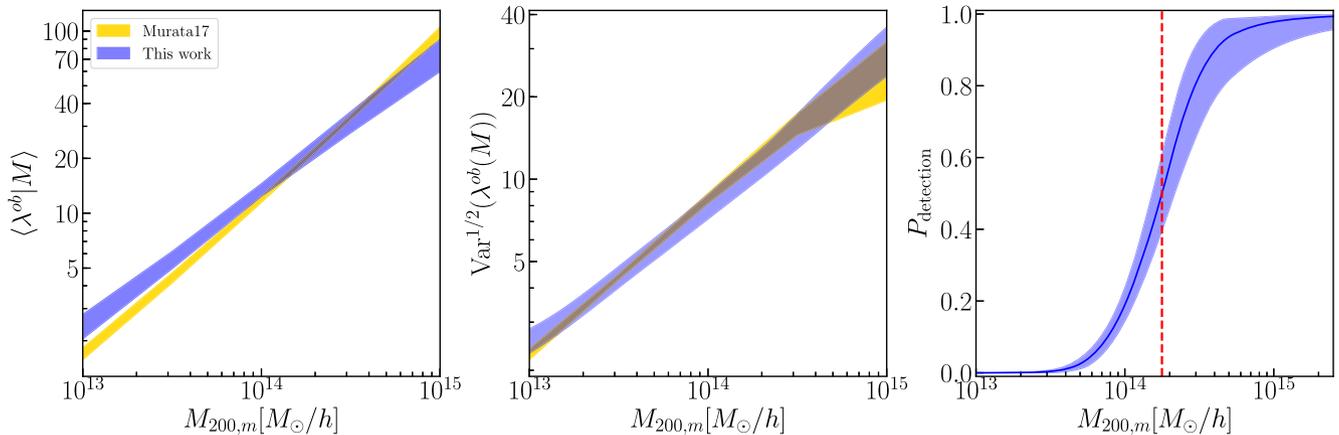
Figure 9. Observable–mass relation and mass-selection function of the redMaPPer catalogue assuming our reference richness–mass relation model (equation 9) at the mean sample redshift $z = 0.22$. *Left-hand* panel: Expectation value for the observed richness as a function of mass. *Central* panel: Scatter of λ^{ob} – Var$^{1/2}(\lambda^{ob}|M)$ – as a function of mass. *Right-hand* panel: Detection probability as a function of cluster mass. The *dashed* vertical line correspond to the mass at which the detection probability is 50 per cent (log $M_{50\,\mathrm{per\,cent}} = 14.24[\mathrm{M}_\odot\,h^{-1}]$). The *blue* area corresponds to the 68 per cent confidence interval derived for the different quantities in this work. For comparison, the results obtained in Murata et al. (2018) are shown in *yellow* in the two left-hand panels.
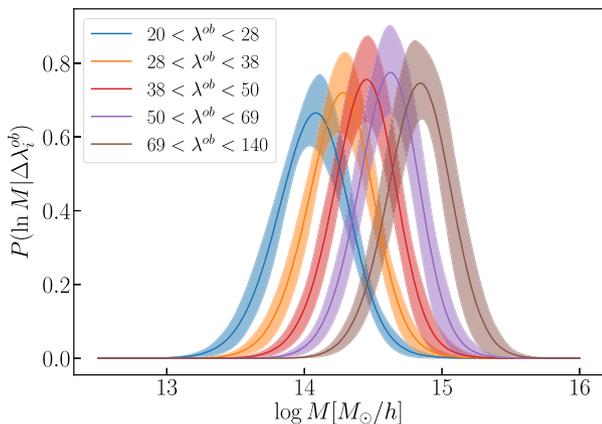
Figure 10. Distribution of halo mass for clusters in each of the five richness bins employed in this work, as labelled. The width of the bands correspond to the 68 per cent confidence interval of the distribution as sampled from our posterior.

(i) BAO data from multiple galaxy surveys, specifically the Six Degree Field Galaxy Survey (6dF; Beutler et al. 2011), the SDSS DR 7 Main galaxy sample (Ross et al. 2015), and data from the Baryon Oscillation Spectroscopic Survey (Alam et al. 2017).

(ii) CMB data from *Planck* satellite, including low l polarization data, from the 2015 data release (hereafter Planck DR15; Planck Collaboration XIII 2016a).

When combining with BAO data we replace the Gaussian prior on h by a flat prior, while when combining with CMB data we relax all the informative priors on cosmological parameters (i.e. h, $\Omega_b\,h^2$, and $\Omega_v\,h^2$, see Table 3) and add the optical depth τ as a free parameter.

According to the protocol detailed in Section 5, both data sets passed the consistency criterion required to perform the combined analysis with the SDSS data. Specifically, for the combination of the BAO and SDSS data sets we checked for consistency between Ω_m posteriors, finding the point $p_{\mathrm{SDSS}} - p_{\mathrm{BAO}} = 0$ to lie within the 96.5 per cent confidence level of the $p_{\mathrm{SDSS}} - p_{\mathrm{BAO}}$ distribution. As for the consistency between Planck DR15 CMB and SDSS data sets we considered the parameters sub-space (Ω_m, σ_8), for which
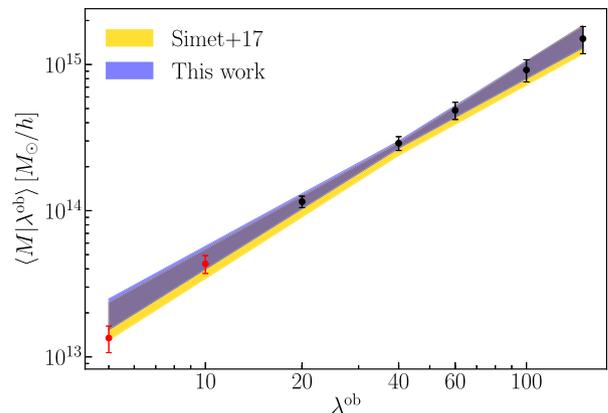
Figure 11. Mass–richness relation derived from the redMaPPer SDSS sample combining cluster abundance and weak lensing data (*blue area*). The data points show the mean mass at a given richness, $\langle M|\lambda^{ob}\rangle$, derived from the posterior distributions of our reference model (see the text for details). In analogy with the analysis of Simet et al. (2017) only the *black* points ($\lambda^{ob} > 20$) are used to fit the mass–richness relation. For comparison the mass–richness relation derived in Simet et al. (2017) is shown in *yellow*.

we found the point $p_{\mathrm{SDSS}} - p_{\mathrm{CMB}} = 0$ to fall within the 85 per cent confidence level distribution of $p_{\mathrm{SDSS}} - p_{\mathrm{CMB}}$.[10]

Fig. 13 shows the 2D marginalized contours for each of the above experiments in the S_8–Ω_m–h parameter sub-space (*left-hand* panels), as well as the posterior for a joint clusters + BAO, and clusters + BAO + Planck analysis (*right-hand* panels). The corresponding 1D marginalized posterior are listed in Table 4.

---

[10]At the time of performing this analysis the latest *Planck* DR18 likelihood is not publicly available. However, the latest *Planck* results (Planck Collaboration VI 2018) are consistent with the previous data release (Planck Collaboration XIII 2016a) (see Fig. 13 for a comparison). According to our consistency criterion, SDSS is consistent also with Planck DR18; specifically we find the $p_{\mathrm{SDSS}} - p_{\mathrm{Planck18}} = 0$ point to lie within the 82 per cent confidence distribution of $p_{\mathrm{SDSS}} - p_{\mathrm{Planck18}}$.
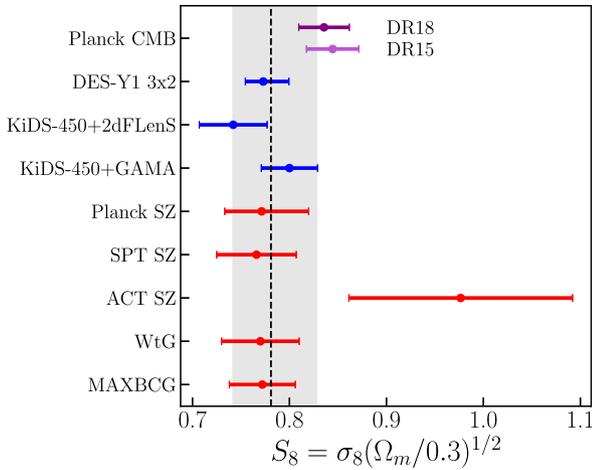
Figure 12. Comparison of the 68 per cent confidence level constraint on S_8 derived from our baseline model (*shaded grey* area) with other constraints from the literature: *red* error bars for cluster abundance analyses, *blue* error bars for weak lensing and galaxy clustering analyses and *purple* for the CMB constraint. From the bottom to the top: MAXBCG from Rozo et al. (2010); WtG from Mantz et al. (2015); ACT SZ from Hasselfield et al. (2013) (BBN+H0 + ACTcl(dyn) in the paper); SPT SZ from de Haan et al. (2016); Planck SZ from Planck Collaboration XXIV (2016b) (CCCP + H_0+BBN in the paper); KiDs-450 + GAMA from van Uitert et al. (2018); KiDs-450 + 2dFLens from Joudaki et al. (2018); DES Y1 3 × 2 from DES Collaboration (2018); *Planck* CMB from Planck Collaboration XIII (2016a) (DR15); and Planck Collaboration VI (2018) (DR18). Note that all the constraints but those from DES Y1 3 × 2 and Planck CMB have been derived fixing the total neutrino mass either to 0 or to 0.06 eV.

The combination of galaxy clusters data and BAO measurements results in a precise measurement of the Hubble parameter, $h = 0.66 \pm 0.02$. This value is in excellent agreement and competitive with those derived from *Planck* DR15 CMB data alone $h = 0.66^{+0.02}_{-0.03}$. By contrast, the posterior of h is in 2.7σ tension with the one derived by the SH0ES collaboration using Type Ia supernovae data, $h = 0.732 \pm 0.017$ (Riess et al. 2016), and in 2.1σ tension with the recent strong-lensing based measurement $h = 0.725^{+0.021}_{-0.023}$ presented in Birrer et al. (2019).

The further inclusion of *Planck* DR15 data significantly improve the constraints on all the cosmological parameters considered. Specifically, the errors on Ω_m, σ_8, and h are reduced compared to the SDSS + BAO analysis by a factor of 4, 3, and 2, respectively. Nevertheless, the low-redshift Universe contributes a significant amount of new information: the errors on Ω_m, σ_8, and h for the joint analysis are reduced relative to the *Planck* DR15-only constraints by a factor of 3.6, 2, and 3, respectively.

It is also interesting to investigate the impact that the *Planck* cosmological information has on the parameters governing the richness–mass relation of the redMaPPer clusters. The error on α is reduced from $\sigma_\alpha = 0.06$ to $\sigma_\alpha = 0.03$, while the error on $\log M_1$ goes from $\sigma_{\log M_1} = 0.09$ to $\sigma_{\log M_1} = 0.02$. The factor of four improvement in the $\log M_1$ posterior after adding *Planck* data suggests that the error budget for mass calibration in cluster abundance studies needs to be reduced from the present ≈ 8 per cent to ≈ 2 per cent for *Planck* to add no information to the cluster abundance constraint on S_8. This value can be compared to the 5 per cent mass calibration achieved by the DES collaboration in McClintock et al. (2019b).

Remarkably, neither the BAO nor the *Planck* data sets improve the posterior on the intrinsic scatter. This may seem surprising

given our earlier discussion on the degeneracy between S_8 and σ_{intr}: if tightening the scatter prior improves the S_8 posterior, why does tightening S_8 not improve the scatter posterior? The resolution is evident from Fig. 7: the *Planck* data tightens S_8 around the value $S_8 = 0.83$. This S_8 value cuts across the mild $S_8–\sigma_{intr}$ degeneracy in such a way that the full range of σ_{intr} values is sampled. Had the *Planck* data favoured either a higher or lower S_8, the posterior on σ_{intr} would have been reduced.

Finally, we find the addition of cluster data has only a modest impact on the posterior on $\sum m_\nu$ from the combination of *Planck* and BAO data. To explore whether future cluster abundance analyses are likely to result in significant improvements we ran chains adopting unrealistically tight 1 per cent priors on the amplitude and slope of the richness–mass relation, as well as a $\sigma_{intr} \leq 0.3$ prior on the scatter. Even in this overoptimistic scenario, clusters had only a minor impact on the posterior for $\sum m_\nu$. This is not entirely unexpected given the small redshift range probed by our cluster catalogue and the fact that the abundance function is only directly sensitive to (1) $\Omega_{cdm} + \Omega_b$ and (2) the amplitude of the dark matter and baryons power spectrum (e.g. Costanzi et al. 2013). While some sensitivity to $\sum m_\nu$ at a given redshift remains via the volume term in the abundance prediction, the sensitivity to neutrino mass at fixed $\Omega_{cdm} + \Omega_b$ and primordial power spectrum amplitude, A_s, is relatively mild.

8 SUMMARY AND CONCLUSION

We have performed a joint analysis of the abundance and weak lensing mass measurements of the redMaPPer clusters identified in the SDSS DR 8 (Aihara et al. 2011) to simultaneously constrain cosmology and the richness–mass relation parameters. The cosmological sample consists of 6964 clusters having richness $\lambda^{ob} \geq 20$ in the redshift range $0.1 < z < 0.3$. For the weak lensing mass estimates we employed the results of the stacked weak lensing analysis performed by Simet et al. (2017), which achieved a 7.7 per cent precision including both statistical and systematic uncertainties (see Table 2). Our analysis is the first cluster abundance study to be performed while blinded to the recovered cosmological parameters. All the modelling choices and validation tests were made before unblinding the cosmological results. We also verified that our cosmological posteriors are robust to assumptions made about the form and parametrization of the richness–mass relation and systematics associated with the calibration of projection effects (see Fig. 8).

Assuming a flat ΛCDM model with massive neutrinos, and including modest H_0 and big bang nucleosynthesis (BBN) priors (Cooke et al. 2016), we found $S_8 = 0.79^{+0.05}_{-0.04}$. Our result is in agreement with those obtained by other cluster abundance studies, as well as with constraints derived from the DES Y1 3 × 2 analysis (DES Collaboration 2018) and *Planck* DR18 CMB data (Planck Collaboration VI 2018). The error budget on S_8 is not dominated by a single set of observables; while mass calibration uncertainties are typically the dominant source of error in cluster abundance studies, the uncertainty in the scatter of the richness–mass relation degrades the constraining power of our sample. Since the detailed shape of the abundance function is sensitive to the scatter, the error budget of the abundance data impacts our S_8 posterior at a level comparable to that from our mass-calibration uncertainty. Future analyses that accurately measure the scatter in the richness–mass relation – e.g. from multiwavelength observations of redMaPPer clusters – will have a significant impact
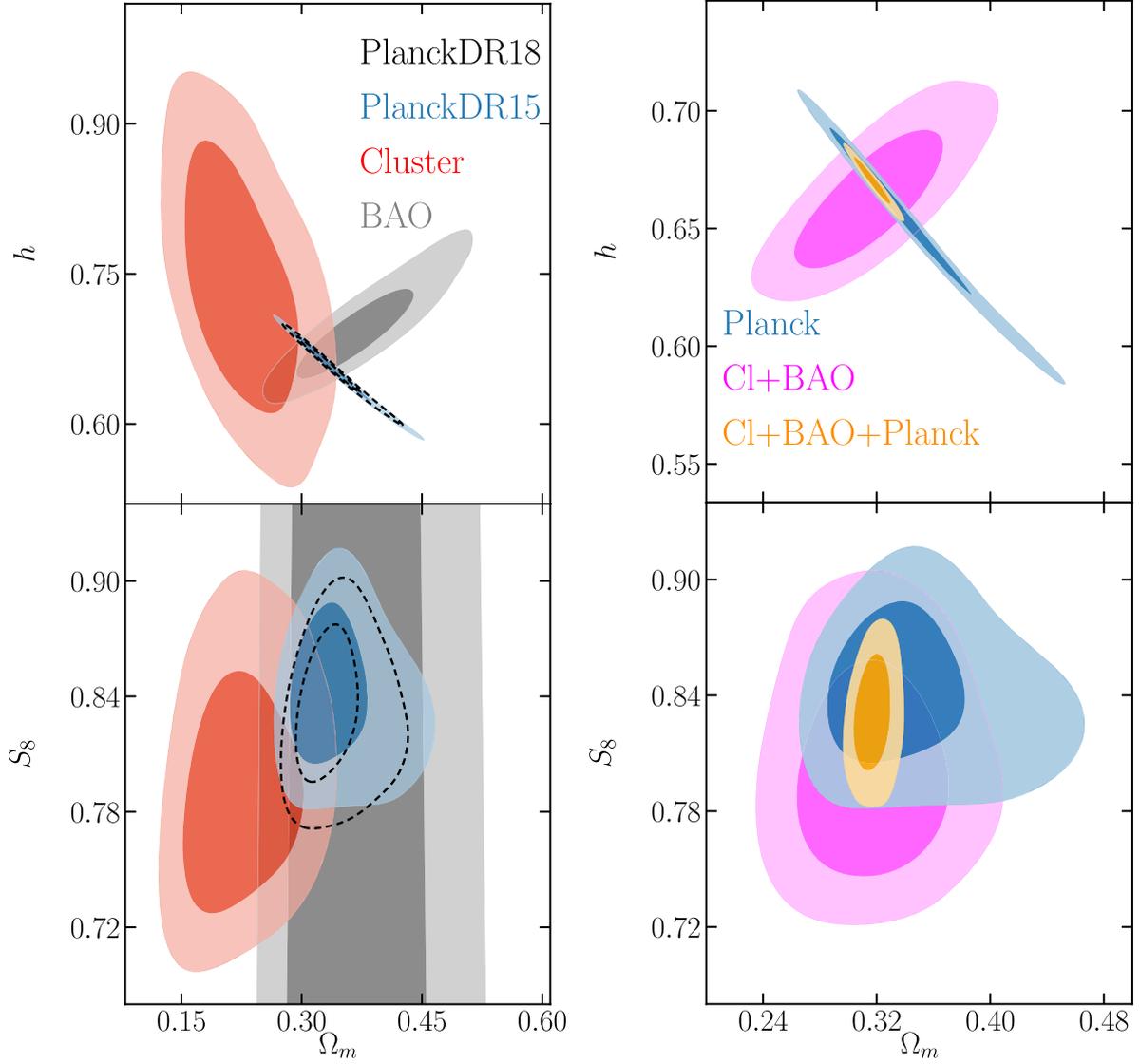
Figure 13. 68 per cent and 95 per cent confidence level constraints in the (S_8, Ω_m, h) plane. *Left-hand* panel: Comparison of the constraints derived from the different data sets considered in this work: *Planck* DR15 (*blue*), BAO (*grey*) and SDSS clusters (*red*). The BAO contours are obtained including the flat prior $\Omega_v\,h^2 \in [0.0006, 0.01]$, as in the SDSS cluster analysis. Also shown for comparison the latest *Planck* results [(Planck Collaboration VI 2018); *dashed black lines*]. *Right-hand* panel: 68 per cent and 95 per cent confidence contours obtained from the combination of the SDSS cluster sample with BAO data (*magenta*) and from the combination of SDSS clusters, BAO, and *Planck* data (*orange*). For comparison, the *blue* contours show the constraints derived from *Planck* CMB data alone. Note the different scales between the *left-hand* and *right-hand* panels.

Table 4. Parameter constraints from the combination of our analysis of the SDSS redMaPPer cluster abundances with BAO and Planck CMB data sets (see the text for details). For reference here are also reported the constraints derived from Planck DR15 CMB and low *l* polarization data (Planck Collaboration XIII 2016a), BAO data (Beutler et al. 2011; Ross et al. 2015; Alam et al. 2017), and SDSS data alone.

Data sets	Ω_m	σ_8	h	S_8	$\log M_{min}$	$\log M_1$	α	σ_{intr}
Planck15	$0.328^{+0.039}_{-0.026}$	$0.81^{+0.03}_{-0.05}$	$0.662^{+0.019}_{-0.028}$	0.841 ± 0.026	—	—	—	—
BAO	0.373 ± 0.053	—	0.694 ± 0.033	—	—	—	—	—
SDSS	$0.22^{+0.05}_{-0.04}$	$0.91^{+0.11}_{-0.10}$	—	$0.79^{+0.05}_{-0.04}$	11.2 ± 0.2	$12.42^{+0.16}_{-0.13}$	$0.65^{+0.05}_{-0.07}$	<0.4
SDSS + BAO	0.316 ± 0.036	0.78 ± 0.06	$0.662^{+0.019}_{-0.022}$	$0.792^{+0.039}_{-0.037}$	11.38 ± 0.17	12.63 ± 0.09	0.76 ± 0.05	<0.2
SDSS + BAO + Planck15	$0.316^{+0.010}_{-0.008}$	0.81 ± 0.02	$0.671^{+0.006}_{-0.008}$	$0.829^{+0.022}_{-0.020}$	11.42 ± 0.15	12.65 ± 0.02	0.76 ± 0.03	<0.2

on the cosmological conclusions that can be drawn from optical cluster samples.[11]

Having ascertained the statistical consistency of our data set with *Planck* DR15 CMB data and BAO priors, we combined the SDSS cluster abundance analysis with these two external data sets. From the joint analysis of SDSS and BAO data we obtain $\Omega_m = 0.32 \pm 0.04$, $\sigma_8 = 0.78 \pm 0.06$, and $h = 0.66 \pm 0.02$. These constraints are consistent with and of comparable size to the CMB constraints from *Planck* data. The further inclusion of the *Planck* DR15 data improves the precision of the parameters S_8, h, and α by a factor of 2 and $\log M_1$ by a factor of 4.5. Adding clusters data to *Planck* + BAO has a negligible impact on the posterior of the sum of the neutrino masses, $\sum m_\nu$. This conclusion holds for local cluster surveys even if cluster mass calibration uncertainties decrease to the percent level. Table 4 summarizes the posteriors of the SDSS clusters after combining with the BAO and *Planck* DR15 external data sets.

We have also compared our posteriors on the richness–mass relation to other analyses. In particular, we find that our posterior for the richness–mass relation is in excellent agreement with the results of Murata et al. (2018), except for the lowest richness bin. That work claims ≈ 10 per cent of the clusters in our lowest richness bin have masses $M \leq 10^{13}\ h^{-1}\,M_\odot$, whereas we find all our clusters have mass $M \gtrsim 2 \times 10^{13}\ h^{-1}\,M_\odot$. We argue that this difference is driven by a theoretical systematic associated with the model adopted in Murata et al. (2018), rather than systematic uncertainties inherent to the data. The stellar mass of the central galaxies in our clusters is consistent with this interpretation. The otherwise excellent agreement between our work and that of Murata et al. (2018) is notable given the significant methodological differences between the two works.

In short, our results are best summarized by saying that the SDSS cluster abundance data is consistent with the best-fitting flat ΛCDM cosmology from *Planck*. Our results are also consistent with but have somewhat larger errors than current state-of-the-art analysis combining the auto- and cross-correlations of galaxies and shear (e.g. DES Collaboration 2018; Joudaki et al. 2018; van Uitert et al. 2018; see Fig. 12). Future analyses that reduce the mass-calibration uncertainties, combined with measurements of the scatter of the richness–mass relations, will make cluster abundances studies competitive with these combined-clustering results. The first demonstration of this coming power will be the upcoming analysis of the DES Y1 data set (DES collaboration, in preparation).

ACKNOWLEDGEMENTS

---

[11] Given an observational mass proxy X that is known a priori to have substantially lower scatter at fixed mass than richness (e.g. gas mass or SZ decrement), one can use the joint distribution $P(\lambda, X)$ of the detected clusters to infer the scatter in richness at fixed mass.

REFERENCES

Aihara H. et al., 2011, ApJS, 193, 29
Alam S. et al., 2017, MNRAS, 470, 2617
Allen S. W., Evrard A. E., Mantz A. B., 2011, ARA&A, 49, 409
Anderson L., et al., 2014, MNRAS, 441, 24
Behroozi P., Wechsler R., Hearin A., Conroy C., 2018, MNRAS, 488, 3143
Behroozi P. S., Wechsler R. H., Wu H.-Y., 2013, ApJ, 762, 109
Berlind A. A., Weinberg D. H., 2002, ApJ, 575, 587
Beutler F. et al., 2011, MNRAS, 416, 3017
Birrer S. et al., 2019, MNRAS, 484, 4726
Bocquet S., Saro A., Dolag K., Mohr J. J., 2016, MNRAS, 456, 2361
Borgani S. et al., 2001, ApJ, 561, 13
Boylan-Kolchin M., Springel V., White S. D. M., Jenkins A., 2010, MNRAS, 406, 896
Brandbyge J., Hannestad S., Haugbølle T., Wong Y. Y. Y., 2010, J. Cosmol. Astropart. Phys., 9, 014
Bullock J. S., Wechsler R. H., Somerville R. S., 2002, MNRAS, 329, 246
Burenin R. A., Vikhlinin A. A., 2012, Astron. Lett., 38, 347
Busch P., White S. D. M., 2017, MNRAS, 470, 4767
Castorina E., Sefusatti E., Sheth R. K., Villaescusa-Navarro F., Viel M., 2014, J. Cosmol. Astropart. Phys., 2, 049
Cataneo M. et al., 2015, Phys. Rev. D, 92, 044009
Charnock T., Battye R. A., Moss A., 2017, Phys. Rev. D, 95, 123535
Cooke R. J., Pettini M., Nollett K. M., Jorgenson R., 2016, ApJ, 830, 148
Costanzi M., Villaescusa-Navarro F., Viel M., Xia J.-Q., Borgani S., Castorina E., Sefusatti E., 2013, J. Cosmol. Astropart. Phys., 12, 012
Costanzi M. et al. 2019, MNRAS, 482, 490
Crocce M., Fosalba P., Castander F. J., Gaztañaga E., 2010, MNRAS, 403, 1353
Cui W., Borgani S., Murante G., 2014, MNRAS, 441, 1769
de Haan T. et al., 2016, ApJ, 832, 95
DeRose J.DES Collaboration, et al., DES Collaboration 2019, preprint. (arXiv:1901.02401)
DeRose J. et al., 2019, ApJ, 875, 69
DES Collaboration, 2018, Phys. Rev. D, 98, 043526
Despali G., Giocoli C., Angulo R. E., Tormen G., Sheth R. K., Baso G., Moscardini L., 2016, MNRAS, 456, 2486
Diemer B., Kravtsov A. V., 2014, ApJ, 789, 1
Diemer B., Kravtsov A. V., 2015, ApJ, 799, 108
Eke V. R., Cole S., Frenk C. S., Patrick Henry J., 1998, MNRAS, 298, 1145
Farahi A., Evrard A. E., Rozo E., Rykoff E. S., Wechsler R. H., 2016, MNRAS, 460, 3900
Feldmann R. et al., 2006, MNRAS, 372, 565
Gelman A., Rubin D. B., 1992, Stat. Sci., 7, 457
Hasselfield M. et al., 2013, J. Cosmol. Astropart. Phys., 7, 008
Henry J. P., 2000, ApJ, 534, 565
Henry J. P., 2004, ApJ, 609, 603
Hikage C., Mandelbaum R., Leauthaud A., Rozo E., Rykoff E. S., 2018, MNRAS, 480, 2689
Hinshaw G. et al., 2013, ApJS, 208, 19
Hirata C., Seljak U., 2003, MNRAS, 343, 459
Hoekstra H., Herbonnet R., Muzzin A., Babul A., Mahdavi A., Viola M., Cacciato M., 2015, MNRAS, 449, 685

Hoffmann K., Bel J., Gaztañaga E., 2015, MNRAS, 450, 1674
Hu W., Cohn J. D., 2006, Phys. Rev. D, 73, 067301
Hu W., Kravtsov A. V., 2003, ApJ, 584, 702
Jiang F., van den Bosch F. C., 2016, MNRAS, 458, 2848
Joudaki S. et al., 2018, MNRAS, 474, 4894
Knebe A. et al., 2013, MNRAS, 435, 1618
Kravtsov A. V., Berlind A. A., Wechsler R. H., Klypin A. A., Gottlöber S., Allgood B., Primack J. R., 2004, ApJ, 609, 35
Kravtsov A. V., Borgani S., 2012, ARA&A, 50, 353
Liu J., Bird S., Zorrilla Matilla J. M., Hill J. C., Haiman Z., Madhavacheril M. S., Petri A., Spergel D. N., 2018, J. Cosmol. Astropart. Phys., 2018, 49
Mana A., Giannantonio T., Weller J., Hoyle B., Hütsi G., Sartoris B., 2013, MNRAS, 434, 684
Mandelbaum R., Hirata C. M., Leauthaud A., Massey R. J., Rhodes J., 2012, MNRAS, 420, 1518
Mandelbaum R., Slosar A., Baldauf T., Seljak U., Hirata C. M., Nakajima R., Reyes R., Smith R. E., 2013, MNRAS, 432, 1544
Mandelbaum R. et al., 2018, MNRAS, 481, 3170
Mantz A., Allen S. W., Rapetti D., Ebeling H., 2010, MNRAS, 406, 1759
Mantz A. B. et al., 2015, MNRAS, 446, 2205
Mao Y.-Y., Williamson M., Wechsler R. H., 2015, ApJ, 810, 21
McClintock T. et al., 2019a, MNRAS, 482, 1352
McClintock T. et al., 2019b, ApJ, 872, 53
Medezinski E. et al., 2018, PASJ, 70, 30
Melchior P. et al., 2017, MNRAS, 469, 4899
Miyatake H. et al., 2019, ApJ, 875, 63
Murata R., Nishimichi T., Takada M., Miyatake H., Shirasaki M., More S., Takahashi R., Osato K., 2018, ApJ, 854, 120
Nakajima R., Mandelbaum R., Seljak U., Cohn J. D., Reyes R., Cool R., 2012, MNRAS, 420, 3240
Navarro J. F., Frenk C. S., White S. D. M., 1997, ApJ, 490, 493
Pierpaoli E., Scott D., White M., 2001, MNRAS, 325, 77
Planck Collaboration VI, 2018, preprint (arXiv:1807.06209)
Planck Collaboration XIII, 2016a, A&A, 594, A13
Planck Collaboration XXIV, 2016b, A&A, 594, A24
Reddick R. M., Wechsler R. H., Tinker J. L., Behroozi P. S., 2013, ApJ, 771, 30
Reiprich T. H., Böhringer H., 2002, ApJ, 567, 716
Reyes R., Mandelbaum R., Gunn J. E., Nakajima R., Seljak U., Hirata C. M., 2012, MNRAS, 425, 2610
Riess A. G. et al., 2016, ApJ, 826, 56
Ross A. J., Samushia L., Howlett C., Percival W. J., Burden A., Manera M., 2015, MNRAS, 449, 835
Rozo E., Rykoff E. S., Becker M., Reddick R. M., Wechsler R. H., 2015, MNRAS, 453, 38
Rozo E. et al., 2010, ApJ, 708, 645
Rykoff E. S. et al., 2014, ApJ, 785, 104
Sheth R. K., Tormen G., 1999, MNRAS, 308, 119
Simet M., McClintock T., Mandelbaum R., Rozo E., Rykoff E., Sheldon E., Wechsler R. H., 2017, MNRAS, 466, 3103
Sohn J., Geller M. J., Rines K. J., Hwang H. S., Utsumi Y., Diaferio A., 2018, ApJ, 856, 172
Springel V., 2005, MNRAS, 364, 1105
Springel V. et al., 2018, MNRAS, 475, 676
Suzuki N. et al., 2012, ApJ, 746, 85
Takada M., Spergel D. N., 2014, MNRAS, 441, 2456
Tinker J., Kravtsov A. V., Klypin A., Abazajian K., Warren M., Yepes G., Gottlöber S., Holz D. E., 2008, ApJ, 688, 709
Tinker J. L., Robertson B. E., Kravtsov A. V., Klypin A., Warren M. S., Yepes G., Gottlöber S., 2010, ApJ, 724, 878
van Uitert E. et al., 2018, MNRAS, 476, 4662
Velliscig M., van Daalen M. P., Schaye J., McCarthy I. G., Cacciato M., Le Brun A. M. C., Dalla Vecchia C., 2014, MNRAS, 442, 2641
Vikhlinin A. et al., 2009, ApJ, 692, 1033
Villaescusa-Navarro F., Marulli F., Viel M., Branchini E., Castorina E., Sefusatti E., Saito S., 2014, J. Cosmol. .Astropart. Phys., 3, 011
von der Linden A. et al., 2014a, MNRAS, 439, 2

von der Linden A. et al., 2014b, MNRAS, 443, 1973
Wechsler R. H., Tinker J. L., 2018, ARA&A, 56, 435
Zehavi I. et al., 2011, ApJ, 736, 59
Zhang Y. et al., 2019, MNRAS, 487, 2578
Zheng Z. et al., 2005, ApJ, 633, 791
Zu Y., Mandelbaum R., Simet M., Rozo E., Rykoff E. S., 2017, MNRAS, 470, 551

APPENDIX A: CLUSTER NUMBER COUNTS COVARIANCE MATRIX

The covariance matrix for the cluster number counts is computed adding the different contributions listed in Section 3.3:

$$C = C^{\mathrm{Poisson}} + C^{\mathrm{SampVar}} + C^{\mathrm{Misc}}. \tag{A1}$$

The first two terms, which account for the statistical uncertainty, are computed analytically along the MCMC for the relevant cosmological and model parameters. The Poisson contribution to the covariance matrix is simply given by the expectation value for the number counts in the specific bin (cf. equation 2):

$$C^{\mathrm{Poisson}} = \delta_{ii} \langle N \rangle_i. \tag{A2}$$

The sample variance terms read (Hu & Kravtsov 2003)

$$C^{\mathrm{SampVar}}_{ij} = \left\langle bN \left(\Delta \lambda_i^{\mathrm{ob}}, \Delta z_i^{\mathrm{ob}} \right) \right\rangle \left\langle bN \left(\Delta \lambda_j^{\mathrm{ob}}, \Delta z_j^{\mathrm{ob}} \right) \right\rangle \sigma^2(V_i, V_j). \tag{A3}$$

where the first two terms are defined as

$$
\begin{aligned}
\langle bN(\Delta \lambda_i^{\mathrm{ob}}, \Delta z_i^{\mathrm{ob}}) \rangle &= \int_0^\infty dz^{\mathrm{true}} \, \Omega_{\mathrm{mask}} \frac{dV}{dz^{\mathrm{true}} d\Omega} \\
&\times \int_{\Delta z_i^{\mathrm{ob}}} dz^{\mathrm{ob}} \, P(z^{\mathrm{ob}}|z^{\mathrm{true}})_{\Delta \lambda_i^{\mathrm{ob}}} \\
&\times \int dM b(M, z) \, n(M, z) \\
&\times \int_{\Delta \lambda_i^{\mathrm{ob}}} d\lambda^{\mathrm{ob}} P(\lambda^{\mathrm{ob}}|M, z),
\end{aligned}
\tag{A4}
$$

and the last one corresponds to the rms variance of the linear density field:

$$\sigma^2(V_i, V_j) = \int \frac{d\mathbf{k}}{(2\pi)^3} \sqrt{P_L(k, z_i) P_L(k, z_j)} W_i(\mathbf{k}) W_j(\mathbf{k}). \tag{A5}$$

Here, $b(M, z)$ is the linear halo bias for which we use the Tinker et al. (2010) formula, V_i is the comoving volume corresponding to the redshift bin z^{ob}, and $W_i(\mathbf{k})$ the Fourier transform of the window function. Approximating the survey mask with a top-hat window symmetric around the azimuthal axis, and setting the angular area $\Omega_{\mathrm{mask}} = 2\pi(1 - \cos(\theta_s))$ equal to the total survey area, $W_i(\mathbf{k})$ reads

$$
\begin{aligned}
W_i(\mathbf{k}) &= \left(\frac{dV}{d\Omega}\Big|_{\Delta z_i} \right)^{-1} \int_{\Delta z_i} dz \frac{dV}{dz d\Omega} 4\pi \\
&\times \sum_{l=0}^\infty \sum_{m=-l}^l (i)^l j_l(k\chi(z)) Y_{l,m}(\hat{k}) K_l,
\end{aligned}
\tag{A6}
$$

where $j_l(x)$ are the spherical Bessel functions, $\chi(z)$ is the comoving distance to redshift z, $Y_{l,m}(\hat{k})$ are the spherical harmonics, and K_l the coefficients of the expansion in spherical harmonics of the angular part of the window function:

$$\text{for} \quad l = 0 \qquad K_l = \frac{1}{2\sqrt{\pi}}$$

$$\text{for} \quad l \neq 0 \qquad K_l = \sqrt{\frac{\pi}{2l+1}} \frac{P_{l-1}(\cos(\theta_s)) - P_{l+1}(\cos(\theta_s))}{\Omega_{\mathrm{mask}}}, \tag{A7}$$

where $P_l(x)$ are the Legendre polynomials.

Finally, the term due to the miscentring correction, C^{Misc}, is estimated numerically from 1000 realizations of the number counts data (corrected for the miscentring error) obtained sampling the offset distribution parameters from their priors as described in Zhang et al. (2019).

APPENDIX B: SKEW-NORMAL APPROXIMATION

The richness–mass relation $P(\lambda^{\mathrm{true}}|M)$ is a convolution of a Poissonian and a Gaussian distribution. In this work, we approximate the resulting convolution with a skew-normal distribution:

$$P(\lambda^{\mathrm{true}}|M) = \frac{1}{\sqrt{2\pi\sigma^2}} e^{-\frac{(\lambda^{\mathrm{true}} - \langle \lambda^{\mathrm{sat}}|M \rangle)^2}{2\sigma^2}} \mathrm{erfc}\left[-\alpha \frac{\lambda^{\mathrm{true}} - \langle \lambda^{\mathrm{sat}}|M \rangle}{\sqrt{2\sigma^2}} \right]. \tag{B1}$$

The values of the model parameters α and σ vary as a function of the expectation value $\langle \lambda^{\mathrm{sat}}|M \rangle$ and intrinsic scatter σ_{intr}. We derive these values by fitting the skew-normal distribution to realizations of a normal-Poissonian convolution obtained by varying $\langle \lambda^{\mathrm{sat}}|M \rangle$ and σ_{intr} along the relevant range of values for this analysis. Each $P(\lambda^{\mathrm{true}})$ realization is generated from 10^6 realizations of the true richness obtained as $\lambda^{\mathrm{true}} = 1 + \Delta^{\mathrm{Poisson}} + \Delta^{\mathrm{Gauss}}$, where $\Delta^{\mathrm{Poisson}}$ is a random number drawn from a Poisson distribution having mean $\langle \lambda^{\mathrm{sat}} \rangle$ and Δ^{Gauss} a random number drawn from a Gaussian distribution having null mean and scatter equal to $\sigma_{\mathrm{intr}} \langle \lambda^{\mathrm{sat}} \rangle$. Fig. B1 compares the histograms obtained from these realizations to the resulting best-fitting skew-normal distribution. We calibrate the parameters of the skew-normal distribution along a dense grid in $\langle \lambda^{\mathrm{sat}} \rangle$ and σ_{intr} and linearly interpolate along this 2D grid to define the skew-normal parameters at every point in parameter space.
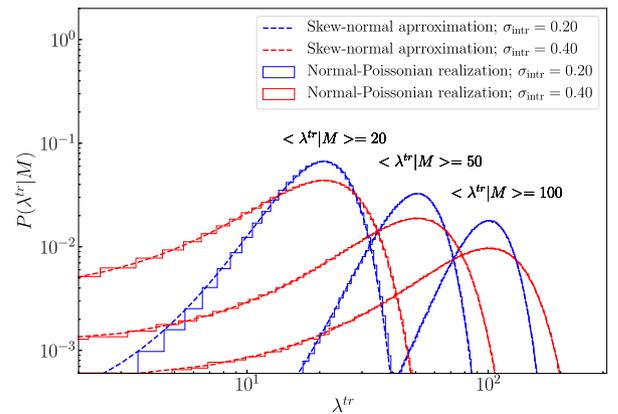

Figure B1. Comparison of the convolution of a normal and Poissonian distribution (*histograms*) with a skew-normal distribution (*solid lines*) for different values of $\langle \lambda^{\mathrm{sat}}|M \rangle$ and σ_{intr} (see labels).

[1]*INAF-Osservatorio Astronomico di Trieste, Via G. B Tiepolo 11, I-34143 Trieste, Italy*

[2]*IFPU-Institute for Fundamental Physics of the Universe, Via Beirut 2, 34014 Trieste, Italy*

[3]*Department of Physics, University of Arizona, Tucson, AZ 85721, USA*

[4]*Department of Physics and Astronomy, University of California Riverside, 900 University Ave, Riverside, CA 92521, USA*

[5]*Fermi National Accelerator Laboratory, PO Box 500, Batavia, IL 60510, USA*

[6]*Department of Astronomy, University of Michigan, Ann Arbor, MI 48109, USA*

[7]*Department of Physics, University of Michigan, Ann Arbor, MI 48109, USA*

[8]*Kavli Institute for Particle Astrophysics & Cosmology, PO Box 2450, Stanford University, Stanford, CA 94305, USA*

[9]*SLAC National Accelerator Laboratory, Menlo Park, CA 94025, USA*

[10]*Santa Cruz Institute for Particle Physics, Santa Cruz, CA 95064, USA*

[11]*Department of Physics, Stanford University, 382 Via Pueblo Mall, Stanford, CA 94305, USA*

[12]*Department of Physics and Astronomy, Pevensey Building, University of Sussex, Brighton BN1 9QH, UK*

[13]*Department of Physics and Astronomy, Stony Brook University, Stony Brook, NY 11794, USA*

[14]*Department of Physics, Carnegie Mellon University, Pittsburgh, PA 15312, USA*

[15]*Max Planck Institute for Extraterrestrial Physics, Giessenbachstrasse, D-85748 Garching, Germany*

[16]*Excellence Cluster Universe, Boltzmannstr 2, D-85748 Garching, Germany*

[17]*Cerro Tololo Inter-American Observatory, National Optical Astronomy Observatory, Casilla 603, La Serena, Chile*

[18]*Department of Physics & Astronomy, University College London, Gower Street, London WC1E 6BT, UK*

[19]*Department of Physics and Electronics, Rhodes University, PO Box 94, Grahamstown 6140, South Africa*

[20]*Institute of Cosmology & Gravitation, University of Portsmouth, Portsmouth PO1 3FX, UK*

[21]*LSST, 933 North Cherry Avenue, Tucson, AZ 85721, USA*

[22]*Laboratório Interinstitucional de e-Astronomia – LIneA, Rua Gal. José Cristino 77, Rio de Janeiro, RJ 20921-400, Brazil*

[23]*Observatório Nacional, Rua Gal. José Cristino 77, Rio de Janeiro, RJ 20921-400, Brazil*

[24]*Department of Astronomy, University of Illinois at Urbana-Champaign, 1002 W. Green Street, Urbana, IL 61801, USA*

[25]*National Center for Supercomputing Applications, 1205 West Clark St., Urbana, IL 61801, USA*

[26]*Institut de Física d'Altes Energies (IFAE), The Barcelona Institute of Science and Technology, Campus UAB, E-08193 Bellaterra (Barcelona), Spain*

[27]*Institut d'Estudis Espacials de Catalunya (IEEC), E-08193 Barcelona, Spain*

[28]*Institute of Space Sciences (ICE, CSIC), Campus UAB, Carrer de Can Magrans, s/n, E-08193 Barcelona, Spain*

[29]*Centro de Investigaciones Energéticas, Medioambientales y Tecnológicas (CIEMAT), 28040 Madrid, Spain*

[30]*Universitäts-Sternwarte, Fakultät für Physik, Ludwig-Maximilians Universität München, Scheinerstr 1, D-81679 München, Germany*

[31]*Department of Astronomy/Steward Observatory, 933 North Cherry Avenue, Tucson, AZ 85721-0065, USA*

[32]*Jet Propulsion Laboratory, California Institute of Technology, 4800 Oak Grove Dr., Pasadena, CA 91109, USA*

[33]*Kavli Institute for Cosmological Physics, University of Chicago, Chicago, IL 60637, USA*

[34]*Instituto de Fisica Teorica UAM/CSIC, Universidad Autonoma de Madrid, E-28049 Madrid, Spain*

[35]*Institute of Astronomy, University of Cambridge, Madingley Road, Cambridge CB3 0HA, UK*

[36]*Kavli Institute for Cosmology, University of Cambridge, Madingley Road, Cambridge CB3 0HA, UK*

[37]*Department of Physics, ETH Zurich, Wolfgang-Pauli-Strasse 16, CH-8093 Zurich, Switzerland*

[38]*Center for Cosmology and Astro-Particle Physics, The Ohio State University, Columbus, OH 43210, USA*

[39]*Department of Physics, The Ohio State University, Columbus, OH 43210, USA*

[40]*Harvard-Smithsonian Center for Astrophysics, Cambridge, MA 02138, USA*

[41]*Australian Astronomical Observatory, North Ryde, NSW 2113, Australia*

[42]*Departamento de Física Matemática, Instituto de Física, Universidade de São Paulo, CP 66318, São Paulo, SP, 05314-970, Brazil*

[43]*Department of Physics and Astronomy, University of Pennsylvania, Philadelphia, PA 19104, USA*

[44]*Department of Physics and Astronomy, George P. and Cynthia Woods Mitchell Institute for Fundamental Physics and Astronomy, Texas A&M University, College Station, TX 77843, USA*

[45]*Department of Astronomy, The Ohio State University, Columbus, OH 43210, USA*

[46]*Institució Catalana de Recerca i Estudis Avançats, E-08010 Barcelona, Spain*

[47]*Brookhaven National Laboratory, Bldg 510, Upton, NY 11973, USA*

[48]*School of Physics and Astronomy, University of Southampton, Southampton SO17 1BJ, UK*

[49]*Physics Department, Brandeis University, 415 South Street, Waltham, MA 02453, USA*

[50]*Instituto de Física Gleb Wataghin, Universidade Estadual de Campinas, 13083-859 Campinas, SP, Brazil*

[51]*Computer Science and Mathematics Division, Oak Ridge National Laboratory, Oak Ridge, TN 37831, USA*

This paper has been typeset from a TEX/LATEX file prepared by the author.